Mon. Not. R. astr. Soc. (1990) **245**, 217–237

Line-strengths in early-type galaxies

J. Gorgas,[1] G. Efstathiou[2] and A. Aragón Salamanca[3]

[1] *Departamento de Astrofísica. Facultad de Físicas, Universidad Complutense, 28040 Madrid, Spain*
[2] *Department of Astrophysics, Keble Road, Oxford OX1 3RH*
[3] *Department of Physics, South Road, Durham DH1 3LE*

Accepted 1990 February 13. Received 1990 January 29; in original form 1989 June 29

SUMMARY

We have analysed Mg, Hβ and Fe line-strengths in a sample of elliptical, S0 and brightest cluster galaxies. For 15 galaxies, our spectra extend to approximately the half-light radius (r_e), and we are able to measure radial line-strength gradients. The metallic line-strength gradients vary markedly from object to object, and do not correlate strongly with parameters such as total luminosity and rotation, though we find some evidence that gradients in the Mg_2 index correlate with central velocity dispersion and central line-strength. The highly variable line-strength gradients in early-type galaxies *shows that they have experienced different star formation histories.* We suggest that this may be explained if they formed by the mergers of subunits in which star formation had proceeded to varying degrees of completion. We find that the line-strengths at $r \sim r_e$ in elliptical galaxies are slightly larger than those of metal-rich galactic globulars, suggesting that typical elliptical galaxies have roughly solar abundance at $r \sim r_e$ and therefore that most ellipticals have relatively weak abundance gradients. The relative line-strengths in the outer parts of ellipticals differ from those in the nuclei of low-luminosity ellipticals, indicating that these stellar populations do not represent a simple one-parameter family governed by mean metal abundance. We find no significant differences in the central Mg and Fe line-strengths of the brightest cluster galaxies and normal ellipticals with the same central velocity dispersion. However, we find that two cD galaxies show Hβ in emission and are also at the centres of the prodigious cooling flows with mass-deposition rates of $\gtrsim 100\,M_\odot\ \mathrm{yr}^{-1}$. Galaxies with cooling flows have identical Mg and Fe line-strengths to galaxies without cooling flows. We show that this implies that only a small fraction of the total luminosity of cooling flow galaxies could come from ongoing star formation with a normal stellar initial mass function.

1 INTRODUCTION

Over the last 25 yr, it has been reasonably well-established that the centres of early-type galaxies are more metal rich than their outer parts. Several observational methods have been used to investigate radial abundance variations. Wide-band photometry has been used by, e.g. de Vaucouleurs (1961), Tifft (1969), Strom & Strom (1978) and Wirth & Shaw (1983). Narrow-band photometry around strong absorption features like those of Mg, Na and CN has been used by, e.g. Spinrad, Smith & Taylor (1972), Burstein (1979) and Thomsen & Baum (1987). Faber (1977), Faber, Burstein & Dressler (1977), Efstathiou & Gorgas (1985) and others have studied gradients in line-strength indices measured directly from spectra. These studies have provided unambiguous evidence of gradients in strong absorption features. However, only a few features, in a small sample of early-type galaxies, have been studied, and the results have left a number of important questions unanswered. For example, much of the narrow-band work has been limited to the nuclear regions of ellipticals; relatively little is known about line-strength gradients at distances comparable to the half-light radii. The lack of such data is not altogether surprising. Accurate high-resolution spectroscopy at large radii requires long exposures with a two-dimensional detector. In this paper we present the results of a long-term project devoted to a systematic analysis of line-strengths in early-type galaxies.

Metallicity gradients in ellipticals have been thought to be an important discriminator between various models for their formation (but see Section 4). For example, Larson (1974, 1975) argues that dissipative collapse would lead to strong metallicity gradients, while some authors have argued that abundance gradients would be weak if ellipticals formed by

dissipationless collapse (e.g. Gott 1975) or by galaxy mergers (Toomre 1977; *cf.* Ostriker 1980). However, before we can make a direct comparison between theoretical models and real galaxies, we require a calibration between line-strengths and metallicity. For an unresolved composite stellar population this is extremely complicated because variations in age and the initial mass function can also produce gradients in the strengths of spectral features.

The Mg_2 index defined by Faber *et al.* (1977), which measures the strength of the Mgb triplet and the band-head of MgH, has been used as a metallicity indicator by many authors (e.g. Terlevich *et al.* 1981; Efstathiou & Gorgas 1985; Thomsen & Baum 1987). This is partly justified by Mould's (1978) theoretical analysis, which showed that the Mg_2 index in an old ($\sim$13 Gyr) stellar population is sensitive to metallicity and insensitive to the shape of the stellar initial mass function. This is fortunate, because the Mgb feature is strong and so is relatively easy to measure at large radii in ellipticals. Much of our analysis is therefore based on measurements of the Mg_2 index, though we present some results from measurements of weaker lines. The best that can be done at present is to summarize the spectral characteristics of ellipticals at large radii by a few line-indices. Our main aims are as follows.

(i) To investigate whether Mg_2 gradients in ellipticals show any regularities, and whether they correlate with other parameters such as luminosity, velocity dispersion, ellipticity, etc. Any such regularities, or lack thereof, could provide important clues to the formation of elliptical galaxies.

(ii) Apart from the Mg_2 index, we have measured line-strengths for the iron blends at 5270 and 5335 Å. The importance of measuring iron peak features has been stressed by Faber (1983) for it supplies a test of the 'lockstep' hypothesis, in which the abundance ratios of all metals relative to hydrogen are assumed to vary in unison (i.e. no selective over-enhancements).

(iii) Several studies have indicated that the stellar populations in globular clusters and elliptical galaxies do not represent a one-parameter family in which metallicity is the key variable (see Burstein 1985, for a review). For instance, the Balmer lines in the nuclei of ellipticals are much stronger than in galactic globular clusters with similar values of Mg_2 (Burstein *et al.* 1984, hereafter BFGK). Several explanations have been proposed to account for these enhanced Balmer line-strengths. Gunn, Stryker & Tinsley (1981) argued for a modest rate of current star formation in the nuclei of ellipticals whereas O'Connell (1980), Pickles (1985) and Rose (1985) argue that the stellar populations in ellipticals contain a substantial intermediate age component. In the outer parts of some of our galaxies, the Mg_2 values fall to 0.1–0.2 mag, i.e. roughly overlapping the range seen in metal-rich galactic globular clusters. We can therefore compare the line-strengths of several absorption features (including the iron blends and Hβ) directly with BFGK's measurement for galactic globular clusters (see also Efstathiou & Gorgas 1985). We can also check whether the strengths of different features vary *within* galaxies according to the same relations that BFGK find for the nuclei of ellipticals, as should be the case if the spectral characteristics of elliptical galaxies were fixed by only one parameter.

(iv) We have measured line-strength gradients in two luminous, bulge dominated, S0 galaxies and three cD galaxies. To a limited extent, we can check whether spectral properties depend on morphological characteristics.

(v) The origin of cD galaxies is still controversial (see White 1983; Dressler 1984). If they formed by the accretion of less-massive-cluster members (Ostriker 1977; Hausman & Ostriker 1978), one might expect to find differences in their line-strengths compared to normal luminous ellipticals (perhaps a dilution of their central line-strengths or weaker gradients). The large gas accretion rates inferred from X-ray observations of cooling flows in rich clusters (Silk 1976; Fabian *et al.* 1981) might play an important role in the formation of cD galaxies and could lead to observable effects in their optical spectra (Sarazin & O'Connell 1983; Johnstone, Fabian & Nulsen 1987). We test some of these points using spectra of the central regions of several brightest cluster galaxies, some of which are at the centres of cooling flows in which high gas-accretion rates have been inferred.

The galaxy sample of our data reduction techniques are described in Section 2. The nuclear line-strength of ellipticals and brightest cluster galaxies are discussed and compared in Section 3. The implications of ongoing star formation in cooling flow galaxies are also discussed in Section 3. Results on line-strength gradients are presented in Section 4 and our conclusions are summarized in Section 5. Tables of line-strengths for each galaxy are given in an Appendix. Some of the main conclusions from our work have been summarized by Gorgas & Efstathiou (1987).

2 OBSERVATIONAL DATA AND REDUCTION

2.1 The data

Most of the galaxy spectra used in this paper were obtained with the Image Photon Counting System (IPCS) at the Anglo-Australian Telescope (AAT) by one of the authors together with various collaborators. The primary purpose of these observations was to measure rotational velocities and velocity-dispersion profiles, and the results may be found in the original papers. The galaxies observed in Run 1 (Efstathiou, Ellis & Carter 1980) were chosen to be nearby 'normal' luminous elliptical galaxies, and were observed with the slit placed along both major and minor axes; a very long major-axis exposure of one of these galaxies (NGC 5813) was taken in Run 2 (Efstathiou *et al.* 1980) to determine the velocity-dispersion profile at large radii. In Run 3, we observed a number of ellipticals of low intrinsic luminosity to test whether the rotational properties of ellipticals depend on absolute magnitude (Davies *et al.* 1983). Observations of two S0 galaxies of high intrinsic luminosity were made in Run 4 in collaboration with D. Carter and R. S. Ellis, and results on their kinematic properties can be found in Gorgas (1987). Three cD galaxies were observed in Run 5 (Carter *et al.* 1985) to test whether their velocity dispersions would increase or decrease with increasing radius. A brief summary of the sample is given in Table 1. To simplify the subsequent discussion, we will refer to each set of observations by the run numbers listed in Table 1.

We have also analysed observations of the central parts of several brightest cluster galaxies (Run 6 in Table 1). These data were obtained with the 1.9-m telescope of the South

Table 1. Summary of observations.

	Galaxy	Type	Exposure (secs)	Comments
Run 1	NGC 4472	E2	3200	Wavelength range: 5000 – 6000 Å
	NGC 4472*		3100	Dispersion: 34 Å/mm
	NGC 5813	E2	4100	Slit width: 3.0″
	NGC 5813*		4000	Flux standard: L970-30
	IC 4296	E1	5000	Reference: Efstathiou *et al.*(1980)
	IC 4296*		5000	Note: Observations marked with * were made along the minor axis.
Run 2	NGC 5813	E2	34200	Wavelength range: 4200 – 5540 Å Dispersion: 33 Å/mm Slit width: 3.0″ Flux standards: L749B & L930-80 Reference: Efstathiou *et al.*(1982)
Run 3	NGC 3818	E3	10650	Wavelength range: 4650 – 5670 Å
	NGC 3904	E3	7200	Dispersion: 33 Å/mm
	NGC 4478	E1	9600	Slit width: 2.0″
	NGC 4742	E3	8700	Flux standards: GD190 & WD485A
	NGC 5638	E1	7800	Reference: Davies *et al.*(1983)
	NGC 5831	E1	7200	
	NGC 5845	E3	9450	
	NGC 3136	E3	1000	
	NGC 3605	E4	1000	
	NGC 3608	E2	1000	
	NGC 3923	E3	1000	
	NGC 3962	E1	1000	
	NGC 4458	E0	1500	
	NGC 4476	E3	1000	
	NGC 4489	E0	1200	
Run 4	IC 4329	S0	4500	Wavelength range: 4870 – 6100 Å
	NGC 4382	S0pec	7500	Dispersion: 33 Å/mm Slit width: 2.0″ Flux standard: L749B
Run 5	0559 -40	cD	7400	Wavelength range: 4150 – 6600 Å
	PKS2354-35	cD	10000	Dispersion: 66 Å/mm
	Sersic 40/6	cD	9000	Slit width: 3.4″ Flux standard: HZ14 Reference: Carter *et al.*(1985)
Run 6	NGC 1316	cD	1200	Wavelength range: 4600 – 5900 Å
	NGC 1600	E4	3000	Dispersion: 50 Å/mm
	NGC 4472	E2	490	Slit width: 4″
	NGC 4696	cD	5700	Flux standards: EG54 & LTT3864
	NGC 5419	E0	4400	
	A 496	cD	11400	
	A 754	cD	15000	
	A 957	cD	9000	
	A 978	cD	14000	
	S 384	cD	15450	
	S 617	cD	9000	

African Astronomical Observatory (SAAO) by one of the authors in 1982 January to provide a comparison between the nuclear properties of brightest cluster galaxies and those of normal ellipticals. The observations were made with the Image Tube Spectrograph (ITS) and the Reticon Photon Counting System. The wavelength range and dispersion used in this run are listed in Table 1.

In this paper we measure the Mg_1, Mg_2, Hβ, Mgb, Fe5270 (hereafter Fe52) and Fe5335 (hereafter Fe53) indices defined by BFGK. Accurate measurement of these indices, especially at low surface brightness levels, requires careful data reduction. A major part of this project has been devoted to isolating and correcting possible sources of systematic error. Several of these are specific to our particular instrumental configurations and are unlikely to be of general interest. We therefore present a brief summary of our data-reduction techniques and describe various error estimates and comparisons with other work. Appendix A gives estimates of the errors in our measurements from the sources described in this Section. A more complete discussion of the data reduction is given by Gorgas (1987).

2.2 Reduction of AAT data

The line-strength indices are subject to several sources of error. These are described below.

(i) *Photon noise:* to estimate the effects of photon statistics, we added Gaussian noise to the central scans of several galaxies. We chose NGC 5813 (Run 2), 3904, 4478, 4742 (Run 3) and 4382 (Run 4) for this test since they cover a wide range in central line-strength values. For simulated spectra with a mean number of $\langle N_p \rangle = 200$ counts pixel^{-1} the relative errors in the line-strengths are as follows: ($\Delta Mg_2/Mg_2 = 0.03$), ($\Delta H\beta/H\beta = 0.23$), ($\Delta Fe52/Fe52 = 0.11$),

(ΔFe53/Fe53 = 0.14), (ΔMgb/Mgb = 0.08), ($\Delta Mg_1/Mg_1 = 0.05$). We found no significant differences between the runs and the errors behaved approximately as $\langle N_p \rangle^{-1/2}$. In the case of Run 5 (dispersion of 1.2 Å pixel^{-1}), tests using the central spectra indicate that these relative errors should be increased by a factor of 1.3. On the basis of these results, we summed spectra in the outer parts of our galaxies to give a minimum of $\langle N_p \rangle = 250$ counts pixel^{-1}.

(ii) *Flux calibration:* to calibrate the galaxy spectra to an absolute scale we used exposures of the Oke (1974) flux standards listed in Table 1. We decided not to use the standard WD485A since this star has a strong and broad Hβ line which distorts a smooth fit to its continuum. This led to discrepancies of up to 8 per cent in Mg_2 for spectra calibrated with the two standards observed in Run 3. In the case of Run 2, Mg_2 values determined using the two flux standards agree within 0.003 mag. In Runs 1, 4 and 5 only one flux standard was observed. Uncertainties associated with flux calibration lead to nearly constant offsets in the Mg_1 and Mg_2 indices; line-strength gradients are completely unaffected. The atomic line-indices are very insensitive to flux calibration errors since the sidebands span a narrow wavelength range.

The line-strengths measured by BFGK are calibrated using a tungsten lamp. Thus, there is no *a priori* reason to expect that our values are on the same system as theirs. As a check, in Table 2 we compare our central Mg_2 values for the galaxies observed in Runs 1, 2 and 3 with measurements by the Lick group (Davies *et al.* 1987). To mimic approximately the aperture used by the Lick group (1.4 × 4 arcsec) we have binned our spectra into effective aperture sizes of $s \times 4$ arcsec, where s is the slit width for each run (see Table 1). As Table 2 shows (see also Fig. 1), the mean offset is +0.004 mag and the rms dispersion is 0.017 mag. Thus, we find no evidence for a systematic offset in our central Mg_2 values.

(iii) *S-distortion:* the IPCS suffers from S-distortion. This results in changes in the shape of the continuum from one side of the galaxy to the other, which in turn leads to systematic errors in the line-strength indices. We have applied a correction to eliminate this effect by fitting the photon counts and determining the position of the galaxy centre as a function of wavelength. The resulting map of the central position is fitted to a low-order polynomial, which is used to straighten the spectra by linear interpolation along the scan direction. The success of this procedure can be judged by the agreement between line-strength indices measured on either side of a galaxy, especially in the central regions where the errors from other sources are small.

Table 2. Comparison with line-strengths from Davies *et al.* (1987).

Galaxy	Mg_2 (This work)	Mg_2 (Davies *et al.*)	ΔMg_2
NGC 3136	0.298	0.296	+0.002
NGC 3605	0.244	0.227	+0.017
NGC 3608	0.345	0.332	+0.013
NGC 3818	0.345	0.334	+0.011
NGC 3904	0.339	0.329	+0.010
NGC 3923	0.332	0.323	+0.009
NGC 3962	0.312	0.324	−0.012
NGC 4458	0.255	0.241	+0.014
NGC 4472	0.356	0.326	+0.030
NGC 4476	0.153	0.172	−0.019
NGC 4478	0.252	0.269	−0.017
NGC 4489	0.229	0.211	+0.018
NGC 4742	0.209	0.188	+0.021
NGC 5638	0.312	0.335	−0.023
NGC 5813	0.316	0.326	−0.010
NGC 5831	0.292	0.306	−0.014
NGC 5845	0.316	0.322	−0.006
IC 4296	0.360	0.334	+0.026

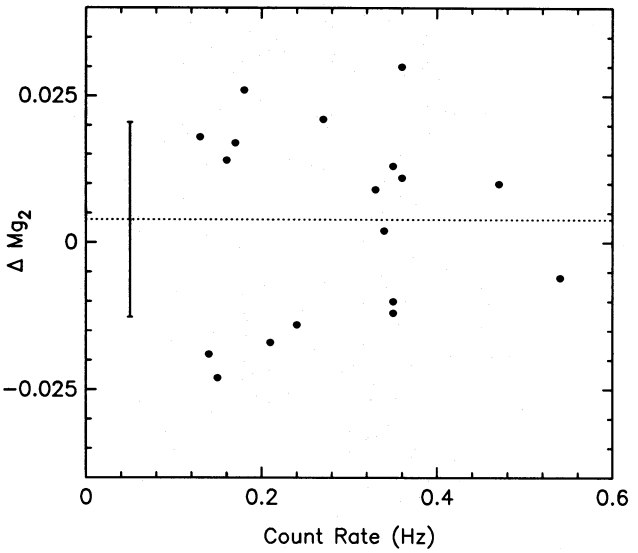

Figure 1. The difference ΔMg_2 between the central Mg_2 indices measured by us and by Davies *et al.* (1987) for the galaxies listed in Table 2 plotted against the mean count rate of our central IPCS spectrum. The dotted line shows the mean value of ΔMg_2 and the error bar shows ± one standard deviation of the data points about the mean line. No trend with count rate is seen, indicating that our results are unaffected by saturation of the IPCS.

(iv) *Sky subtraction:* since the light levels in the outer parts of these galaxies are close to the sky brightness, it is important to quantify errors associated with sky subtraction. The galaxies in Runs 1, 2, 4 and 5 have large angular diameters, so separate sky frames were taken at regular intervals during the night. Most of the galaxies in Run 3 have small diameters, hence spectra in the outermost of each frame are essentially free of contamination by the galaxy and can be used for sky subtraction. To get quantitative estimates of the errors caused by sky subtraction, we varied the sky level for a few galaxies in the sample. The results show that 10 per cent errors in the sky lead to the following relative errors in the line-strength of the outermost spectra: ($\Delta Mg_2/Mg_2 \approx 0.07$), ($\Delta H\beta/H\beta \approx 0.15$), ($\Delta$Fe52/Fe52 ≈ 0.04), ($\Delta$Fe53/Fe53 ≈ 0.06), ($\Delta$Mgb/Mgb ≈ 0.14), ($\Delta Mg_1/Mg_1 \approx 0.02$).

A second effect which is potentially important at low light levels is associated with large-scale variations in the response of the IPCS in both the wavelength and the scan directions. To check for such variations, we used either long sky exposures or twilight sky exposures. These frames were binned to form a course grid of typically 50 bins in the wavelength direction by 20 in the spatial direction. The entire frame was then divided by the central sky spectrum. These tests show that the IPCS response is flat (to within about 2 per cent) over most of the frame area, but declines steeply

towards the edges and corners. For each night's data, we can easily delineate the portion of the frame over which reliable results can be obtained. We have also experimented with a correction for these variations by fitting the normalized sky frames to a low-order polynomial surface which is then used to flatten the object frames. These tests show that even for our outermost data points, non-uniformities in the IPCS response can account for systematic errors of only about 0.02 mag in Mg_2.

(v) *Non-linearity of IPCS:* the mean photon count rate in the central spectrum of NGC 4742 was extremely high (1.7 counts pixel^{-1} s^{-1}). With our configuration, the IPCS overcounts photons at such high count rates, leading to systematically high line-strength indices (see Jenkins 1987, for a thorough discussion of non-linearities in the IPCS). A 1500 s exposure of NGC 4742 was taken through a 0.7 neutral density filter to check for non-linearities in the detector response. Comparison of the spectra taken with and without the ND filter showed systematic errors at high count rates in all of the line-strength indices: for example, Mg_2 was overestimated by 0.1 mag and Fe52 by 1.2 Å in the spectra taken without the ND. By comparing results for spectra away from the nucleus, we found that the non-linearities are a strong function of the photon count rate. At count rates of 0.2 counts pixel^{-1} s^{-1} we find no systematic differences. Unfortunately, the brightness profile of NGC 4742 is too steep to allow an accurate calibration of these effects. The mean count rates in the central spectra for other elliptical galaxies in our sample lie within the range 0.1–0.54 counts pixel^{-1} s^{-1}, so objects at the high end of this range might be mildly affected by non-linearities. Indications that these effects are not serious are provided by Fig. 1 which shows the difference ΔMg_2 between our estimates of Mg_2 and those of Davies *et al.* for the galaxies listed in Table 2 plotted against the mean photon count rate in the central IPCS spectra. There is no evidence of any correlation between differences in central Mg_2 and photon count rates.

(vi) *Velocity dispersions:* some of the line-strength indices are affected by velocity broadening. We have calibrated this effect by convolving stellar spectra with Gaussians. The stars were observed during twilight for subsequent use as templates to measure galaxy rotational velocities and velocity dispersions using Fourier techniques. They span a fairly narrow range of spectral types around K0III. We have averaged the results for 15 stars and determined the following formulae by least-squares minimization:

$$\Delta Mg_2/Mg_2 = 0.0158\sigma_{250}^2 - 0.00343\sigma_{250}, \quad (0.15 < Mg_2 < 0.33), \quad (1a)$$

$$\Delta H\beta = 0.101\sigma_{250}^2 - 0.222\sigma_{250}, (0.91 < H\beta < 2.2), \quad (1b)$$

$$\Delta Fe52/Fe52 = 0.0498\sigma_{250}^2 + 0.0978\sigma_{250}, \quad (3.3 < Fe52 < 5.5), \quad (1c)$$

$$\Delta Fe53/Fe53 = 0.138\sigma_{250}^2 + 0.107\sigma_{250}, \quad (2.9 < Fe53 < 4.4), \quad (1d)$$

$$\Delta Mgb/Mgb = 0.0670\sigma_{250}^2 + 0.111\sigma_{250}, \quad (2.1 < Mgb < 3.8), \quad (1e)$$

$$\Delta Mg_1/Mg_1 = 0.0299\sigma_{250}^2 - 0.0250\sigma_{250}, \quad (0.04 < Mg_1 < 0.28), \quad (1f)$$

where σ_{250} is the velocity dispersion divided by 250 km s^{-1} and the range of line-strengths spanned by the stars is given in brackets. These fits are valid over the range $\sigma < 400$ km s^{-1}. The residual scatter about these mean relations is usually less than 5 per cent. Notice that the atomic line indices Fe52, Fe53 and Mgb are sensitive to broadening, whereas the molecular band indices Mg_1 and Mg_2 are not. We have therefore ignored velocity dispersion corrections in Mg_1 and Mg_2 but have corrected the other indices using equations (1a–f). As a check of our velocity dispersion corrections, we have applied the following test: since Mg_2 is unaffected by broadening, we estimate values for Fe52, Fe53 and Mgb from the mean relations of elliptical nuclei plotted in fig. 5 of BFGK using our estimates of Mg_2; the relative differences between BFGK's measurements (corrected to their instrumental resolution) and our own estimates, uncorrected for broadening, are plotted against central velocity dispersion in Fig. 2. The dotted lines show the trend with velocity

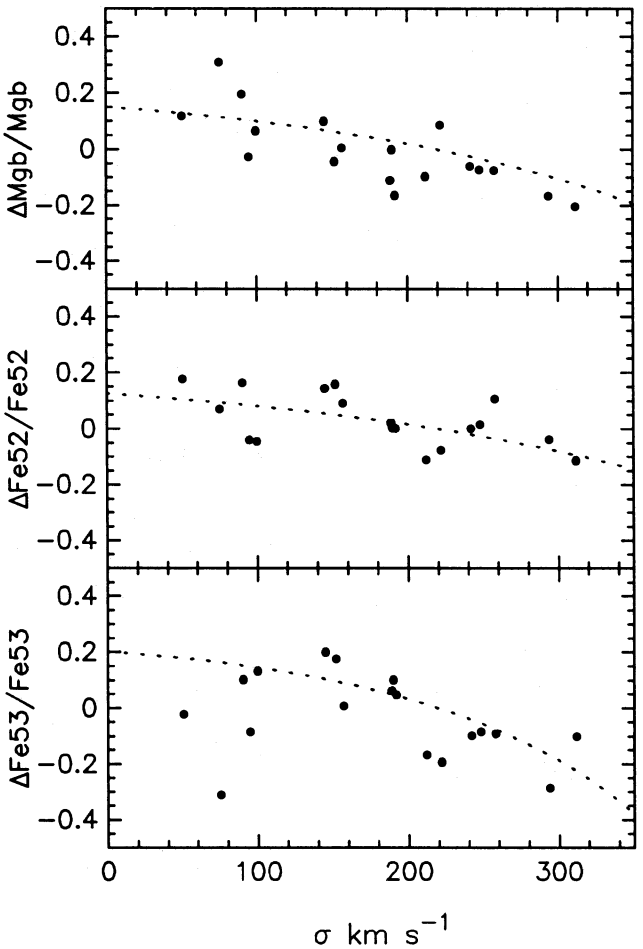

Figure 2. This diagram shows a test of our corrections for velocity dispersion broadening (equations 1a–f) on the values of the Fe52, Fe53 and Mgb indices. For the ellipticals in our sample we have computed the relative difference of our raw measurements (i.e. uncorrected for velocity broadening) and those deduced using our measurements of the Mg_2 index and the mean relations of BFGK for the nuclei of ellipticals (plotted as the solid lines in Fig. 3). The relative difference in the line-strength indices are plotted against central velocity dispersion. The dotted lines show the trends expected from equations (1a–f).

dispersion expected from equations (1a–f). The data points scatter fairly evenly about these lines, showing that our corrections for velocity broadening are reasonably accurate.

(vii) *The Mg_3 index:* the observations of Run 1 lacked part of the spectrum corresponding to the blue side-band of the Mg_2 index. We therefore defined a new index, which we call Mg_3. To avoid the central band of Mg_1 (5071.0–5134.75 Å), without using a band that is too narrow (and thus sensitive to photon noise), we used the mean flux in two separate bands in the blue:

$$\begin{aligned} &\text{blue side-band: } \lambda 5045.0\text{–}5071.0 \text{ Å}, \\ &\qquad\qquad\quad \lambda 5134.75\text{–}5157.0 \text{ Å}, \\ &\text{central band: } \lambda 5157.0\text{–}5198.25 \text{ Å}, \\ &\text{red side-band: } \lambda 5198.25\text{–}5247.0 \text{ Å}. \end{aligned} \qquad (2)$$

The central band corresponds exactly with that of the Mg_2 index but the side-bands are narrower and closer to the Mgb + MgH features. We then calibrated the Mg_3 index against Mg_2 using the galaxies from Runs 2–4. We used all the spectra, from the central regions to the outer parts, thereby allowing an accurate calibration over the range $0.1 < Mg_2 < 0.37$. A least-squares fit gave

$$Mg_2 = (1.808 \pm 0.038)\, Mg_3 - (0.0144 \pm 0.0052) \qquad (3)$$

with an rms scatter of 0.015 mag about this relation. This scatter is small given that some of the spectra have fairly low signal-to-noise ratios. The Mg_3 index is insensitive to velocity broadening.

2.3 Reduction of SAAO data

The SAAO sample includes three normal elliptical galaxies (NGC 1600, 4472 and 5419) which we observed as standards to compare with the results of other authors. The remaining galaxies are cD or brightest cluster membranes (see Section 3.2).

Flat-fielding and wavelength calibration were done with standard software in the same way as the AAT data (e.g. Davies *et al.* 1983). The reticon is a dual channel detector with two apertures separated by 29 arcsec. For the brighter objects, the secondary spectrum was highly contaminated by galaxy light. In such cases, we obtained separate sky exposures offset by ~ 1° which we used for sky subtraction. To calibrate these data, we observed the flux standards EG54 and LTT 3864 (Oke 1974; Stone & Baldwin 1983).

Radial velocities and central velocity dispersions for these galaxies were derived using the Fourier quotient method of Sargent *et al.* (1977) and the cross-correlation method of Tonry & Davis (1979). As a stellar template, we used a composite spectrum of six G8-K0III stars observed during the run. Column (1) of Table 3 lists the mean number of photons pixel^{-1}; columns (2) and (4) list results for the radial velocities and velocity dispersions, respectively, determined from the Fourier quotient method; columns (3) and (5) give the errors determined from the cross-correlation method (see Davies *et al.* 1983). In column (6) we give the central velocity dipersions estimated by other authors. For NGC 1316 we have averaged the velocity dispersions measured by Jenkins & Scheuer (1980), Schweizer (1981) and Bosma, Smith & Wellington (1985). The velocity dispersion for A 496 is from Tonry (1985). The rest of the values are from the catalogue of Davies *et al.* (1987). In all cases, these measurements agree with our results within the errors.

The Mg_2 indices for these galaxies are listed in column (7). The errors in Mg_2 listed in column (8) have been estimated from the uncertainties caused by photon noise, sky subtraction and flux calibration. Column (9) gives Mg_2 indices for four galaxies measured by Davies *et al.* (1987). Their values were measured with a similar sized aperture to ours. so we can directly compare our measurements. The mean offset in Mg_2 between the two sets of measurements is only +0.001 mag and the standard deviation is 0.021 mag, compatible with our estimated errors.

3 CENTRAL LINE-STRENGTHS

3.1 Elliptical galaxies

In Table 4 we list the central line-strength indices for the AAT sample ordered according to the run number. As explained in Section 2.2 these indices have been calculated for an aperture similar to that used by BFGK and have been corrected to a velocity dispersion of 220 km s^{-1} using equations (1a–f) to match their instrumental resolution (*cf.* Fig. 2). In our discussion of line-strength gradients (Section 4), we will frequently refer to BFGK's mean relations between central Mg_2 and other nuclear line-strength indices in ellipticals. It is therefore extremely important to demonstrate that our nuclear values agree with their mean relations, as a check of the validity of these relations and as a further demonstration that our line-strengths are on the same system as theirs. Fig. 3 shows nuclear line-strengths for all of the ellipticals in our sample. We also show the mean of the Fe52 and Fe53

Table 3. Observational parameters for the SAAO galaxies.

Galaxy	N_p (1)	V (2)	ΔV (3)	σ (4)	$\Delta\sigma$ (5)	σ^* (6)	Mg_2 (7)	ΔMg_2 (8)	Mg_2^* (9)
NGC 1316	931	1818	12	254	11	246	0.298	0.018	
NGC 1600	311	4834	22	315	20	326	0.319	0.020	0.331
NGC 4472	120	920	26	287	23	301	0.346	0.025	0.326
NGC 4696	391	3013	23	245	20	231	0.306	0.020	0.289
NGC 5419	527	4165	19	298	17	307	0.331	0.019	0.353
A 496	296	9871	25	264	23	274	0.310	0.020	
A 754	287	16486	22	323	19		0.287	0.022	
A 957	255	13410	24	327	21		0.318	0.015	
A 978	354	16216	19	237	18		0.261	0.019	
S 384	347	18256	26	311	24		0.339	0.022	
S 617	426	10015	16	240	15		0.321	0.022	

Table 4. Central line-strength indices for the AAT galaxies.

Galaxy	Mg_2	$H\beta$	Fe52	Fe53	Mgb	Mg_1
NGC 4472	0.356	–	3.19	3.22	5.20	–
NGC 5813	0.323	–	2.99	2.74	5.05	–
IC 4296	0.360	–	3.41	2.71	5.37	–
NGC 5813	0.309	1.06	2.83	2.38	4.53	0.170
NGC 3818	0.345	1.39	3.18	2.81	4.68	0.182
NGC 3904	0.339	1.56	3.12	2.80	4.43	0.174
NGC 4478	0.252	1.80	3.26	2.88	4.04	0.102
NGC 4742	0.209	3.85	2.50	1.94	2.84	0.096
NGC 5638	0.312	1.54	3.26	2.50	4.63	0.157
NGC 5831	0.292	1.62	3.45	2.93	4.11	0.128
NGC 5845	0.316	1.63	3.19	2.56	4.64	0.155
NGC 3136	0.298	1.98	3.07	2.44	4.37	0.152
NGC 3605	0.244	2.42	3.20	2.41	4.21	0.117
NGC 3608	0.345	1.64	3.18	3.06	5.33	0.173
NGC 3923	0.332	2.22	3.59	2.62	4.91	0.155
NGC 3962	0.312	1.39	2.91	2.33	5.38	0.142
NGC 4458	0.255	1.62	2.62	2.56	3.83	0.115
NGC 4476	0.153	2.45	2.62	1.49	2.97	0.046
NGC 4489	0.229	2.68	3.14	2.02	3.51	0.104
IC 4329	0.400	–	4.45	3.96	4.93	0.229
0559-40	0.318	1.67	2.53	–	4.97	0.154
PKS 2354-35	0.288	-0.07	–	–	5.19	0.143
Sersic 40/6	0.291	1.30	–	2.58	4.77	0.138

indices, ⟨Fe⟩, which has smaller random errors than either of the two iron indices. It is clear from Fig. 3 that our nuclear values obey similar relations to those found by BFGK. The standard deviations of the central indices from these relationships are as follows:

$\sigma(\mathrm{Fe52}) = 0.24,$

$\sigma(\mathrm{Fe53}) = 0.34,$

$\sigma(\mathrm{Mgb}) = 0.42,$

$\sigma(\mathrm{Mg_1}) = 0.009,$

$\sigma(\mathrm{H}\beta) = 0.38,$

$\sigma(\langle\mathrm{Fe}\rangle) = 0.24.$

The scatter in the Fe lines is nearly half that measured by BFGK (their dispersions are indicated by the error bars in Fig. 3). In general, the scatter that we observe is compatible with our estimated measurement errors, with the exception of the $H\beta$–Mg_2 relationship. NGC 4742 provides an extreme example of a discrepancy in $H\beta$ since this galaxy has a central $H\beta$ equivalent width of 3.8 Å. This is nearly twice as large as the average value for an elliptical with similar nuclear metal line-strengths and is indicative of recent (~ 1–2 Gyr) star formation in the nuclear regions. The results shown in

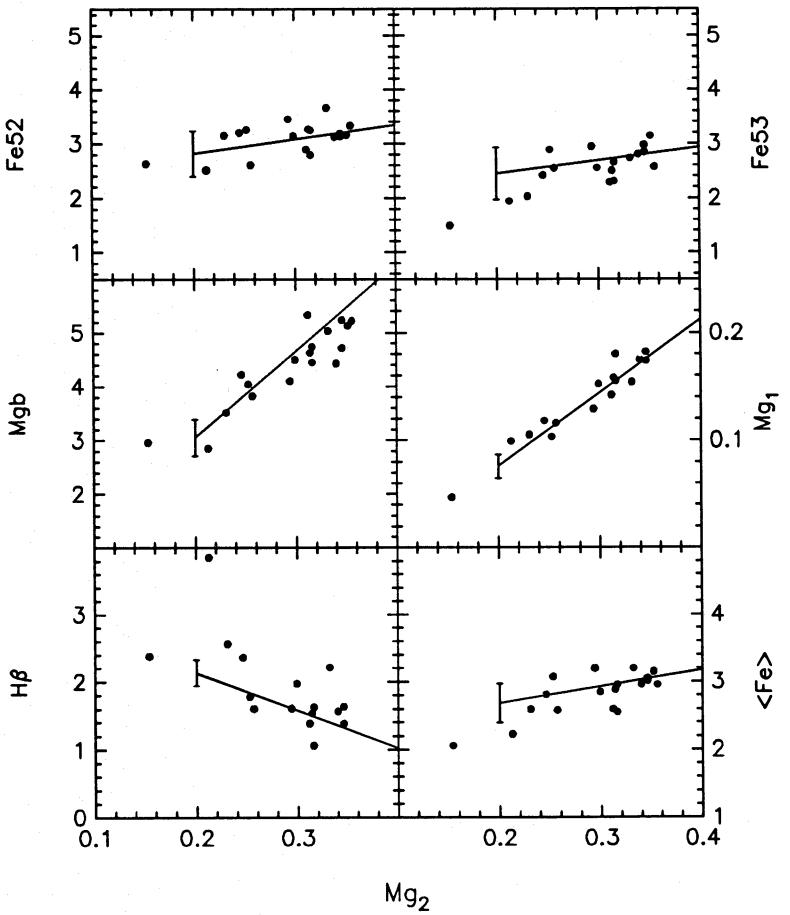

Figure 3. Comparison of nuclear line-strengths for elliptical galaxies in our sample with the mean relations for elliptical nuclei determined by BFGK (solid lines). The error bars show the rms scatter measured by BFGK about each relation. The units of Fe52, Fe53, ⟨Fe⟩, Mgb and $H\beta$ are in Å and those of Mg_1 and Mg_2 are in magnitudes.

Fig. 3 support BFGK's conclusion that the line-strengths in the nuclei of ellipticals obey a well-defined set of relations and that the Hβ line-strengths of ellipticals with low central Mg_2 indices (~ 0.2 mag) are higher than those of metal-rich galactic globular clusters (*cf.* Fig. 11 of this paper or fig. 5 of BFGK). The differences between the line-strengths in the nuclei of low-luminosity ellipticals (e.g. M32) and metal-rich galactic globular clusters have been interpreted as evidence for an intermediate age (~ 5 Gyr) stellar population (see O'Connell 1980; BFGK; Picles 1985; Rose 1985).

Table 5. Corrected parameters for the brightest cluster galaxies.

Galaxy	V	σ_0^c	Mg_2^c	δMg_2^c	Hβ	$\dot{M}$
NGC 1316	1411	242	0.281	−0.024	2.22	
NGC 4696	3041	237	0.294	−0.010	0.75	30
A 496	9877	271	0.320	+0.006	−1.02	120
A 754	16488	350	0.316	−0.017	1.29	24
A 957	13395	345	0.339	+0.007	0.67	
A 978	16201	256	0.286	−0.023	2.06	
S 384	18259	342	0.379	+0.048	0.53	
S 617	10006	246	0.331	+0.025	1.10	
0559-40	13878	295	0.341	+0.021	1.56	
PKS 2354-35	14728	316	0.311	−0.014	−0.19	125
Sersic 40/6	18039	359	0.325	−0.010	1.18	<4.9
NGC 2832	6821	361	0.340	+0.004		
NGC 6086	9547	304	0.344	+0.021		
NGC 6166	8957	326	0.340	+0.012		150
NGC 7720	9416	305	0.339	+0.016		0.0
NGC 7768	7952	242	0.322	+0.017		

Notes to Table 5: The column labelled V gives the heliocentric velocities for the brightest cluster galaxies observed in Runs 5 and 6 and the group velocities from Davies *et al.* (1987) for galaxies in the NGC catalogue. The column labelled Hβ lists our measurements of the Hβ index corrected to zero central velocity dispersion. The column labelled $\dot{M}$ gives the inferred mass deposition rates of cooling gas in solar masses/yr from Edge (1988) and Arnaud & Fabian (private communication).

3.2 Brightest cluster galaxies compared with normal ellipticals

The galaxies observed in Run 6 are mostly dominant cluster galaxies and so we can test whether their nuclear line-strengths are similar to those of normal ellipticals. The sample includes 4 cD galaxies in rich Abell clusters and two cD's in the southern clusters S384 and S617 (Abell, Corwin & Olowin 1989). NGC 1316 is the brightest member of the Fornax cluster and has been classified as a cD by Schweizer (1980). NGC 4696 is the dominant galaxy of the Centaurus cluster.

We have supplemented our sample with the three cD galaxies from Run 5 and with five galaxies from the sample of Davies *et al.* (1987) that are classified as cD's from their luminosity profiles (Schombert 1987) or from their Rood–Sastry types (Struble & Rood 1987). The full list of objects is given in Table 5.

To compare brightest cluster galaxies with normal ellipticals, we have plotted Mg_2 against central velocity dispersion σ_0 (Fig. 4). We have chosen this form of comparison because normal ellipticals show a tight correlation between Mg_2 and central velocity dispersion. A least-squares fit to 456 ellipticals in the Davies *et al.* sample gives

$$Mg_2^c = 0.175 \log \sigma_0^c - 0.112, \qquad (4)$$

with a standard deviation of 0.025 mag in Mg_2. In determining equation (4), we used the aperture corrected values of Mg_2 and σ listed by Davies *et al.*, which correct their observations to an aperture of 4 arcsec at the distance of the Coma cluster. A comparison of our data with equation (4) is preferable to comparing, say, Mg_2 against absolute magnitude. A large fraction of the light in brightest cluster galaxies often comes from an extended envelope, so their absolute magnitudes are difficult to measure. Comparing σ_0 against

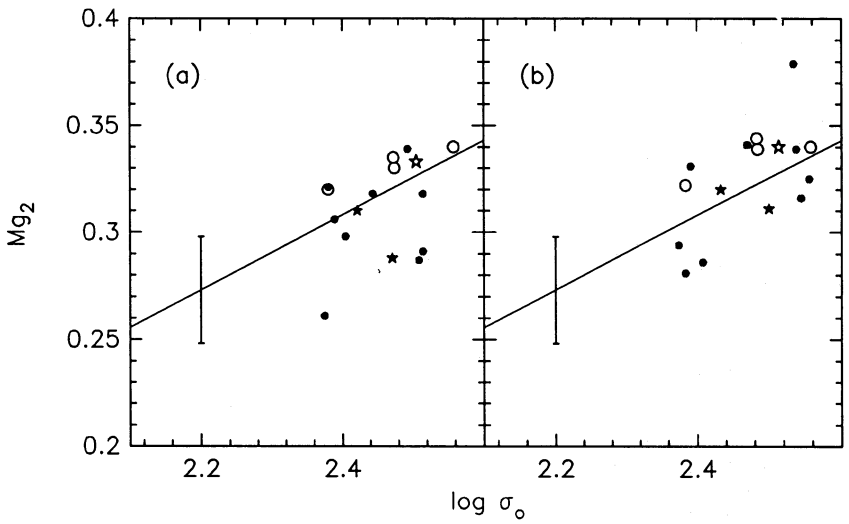

Figure 4. The filled symbols show central Mg_2 values for brightest cluster galaxies observed in Runs 5 and 6 plotted against central velocity dispersions. The open symbols show cD galaxies from the sample of Davies *et al.* (1987). The solid lines show the mean relation for normal elliptical galaxies determined from the sample of Davies *et al.* (equation 4) and the error bars show the standard deviation of Mg_2 about the mean relation. In Fig. 4(a), we have plotted the uncorrected central values listed in Tables 3 and 4. In Fig. 4(b), we have applied the aperture corrections of Davies *et al.* (1987) to correct the measurements to a standard aperture size of 4 arcsec at the distance of the Coma cluster (see Table 5). The galaxies represented by asterisks are at the centres of cooling flows in which mass deposition rates of $> 100\, M_\odot\ \mathrm{yr}^{-1}$ have been inferred.

Mg_2 allows a direct comparison of ellipticals and cD galaxies and avoids the need for accurate surface photometry.

Fig. 4(a) shows the measured Mg_2 indices for brightest cluster galaxies compared with equation (4). Most of the points scatter about the mean relation for ellipticals, but a few appear to have low central Mg_2's for their σ_0. The deviant points tend to have higher redshifts than the others, which suggests that aperture corrections may be necessary. We have therefore applied the aperture corrections of Davies *et al.* (1987) to Mg_2 and σ_0 for our sample. The corrected values are listed in Table 5 and compared with equation (4) in Fig. 4(b). The rms scatter of the corrected Mg_2's around the mean relationship is only 0.020 mag and is slightly smaller than the scatter for normal ellipticals.

The aperture corrections of Davies *et al.* are based on their measurements of nuclear gradients in normal ellipticals and agree well with our results on Mg_2 gradients in ellipticals presented in Section 4. As we show in Section 4, the three cD galaxies of Run 5 possess radial gradients in Mg_2 which are similar, though perhaps weaker, than those of normal ellipticals; the velocity dispersions in these cD galaxies are roughly constant within r_e (Carter *et al.* 1985). If these results apply generally to brightest cluster galaxies, then the aperture corrections of Davies *et al.* would be overestimates and the true relation between Mg_2 and σ_0 might be intermediate to the cases shown in Fig. 4(a) and (b). However, even the uncorrected parameters plotted in Fig. 4(a) show that there is no firm evidence that the Mg_2–σ_0 relation for brightest cluster galaxies differs from that of normal ellipticals.

Fig. 5 shows the central line-strengths (uncorrected for aperture effects) for our sample of brightest cluster galaxies plotted against each other as in Fig. 3. In some of the galaxies we were unable to measure Fe line-strengths because of contamination by night sky emission lines. Within the errors, the cD galaxies obey relations similar to normal ellipticals with the possible exception of galaxies at the centres of cooling flows, which we discuss next.

3.3 Central line-strengths for cooling flow galaxies

The galaxies shown as asterisks in Figs (4) and (5) have precipitous cooling flows, with mass-deposition rates of $\dot{M} > 100\,M_\odot\ \mathrm{yr}^{-1}$ (see Table 5). These galaxies appear normal in the Mg_2–σ_0 diagram, but we find Hβ in emission in the two for which we have been able to measure the Hβ index (Fig. 5).

Emission lines are often observed in cooling flow galaxies (e.g. Heckman 1981; Johnstone *et al.* 1987). Johnstone *et al.* argue that the observed high emission line luminosities can be explained if some of the cooling gas forms stars with a normal initial mass function (IMF). Such star formation may be detectable in spectral features and, in fact, Johnstone *et al.*

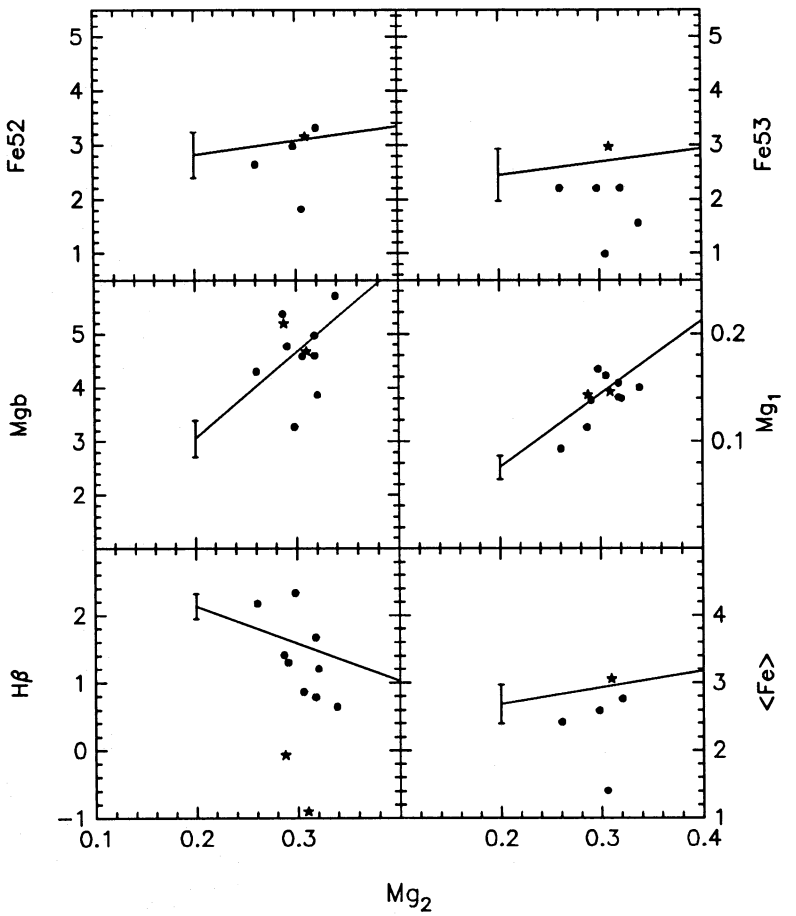

Figure 5. Central line-strengths for brightest cluster galaxies compared with the mean relations for the nuclei of elliptical galaxies as in Fig. 3. The cooling flow galaxies represented by asterisks have mass-deposition rates of $\dot{M} > 100\,M_\odot\ \mathrm{yr}^{-1}$ and show Hβ emission.

presented evidence that the depth of the 4000 Å break (D_{4000}, see Bruzual 1983, for the definition of D) is correlated with $\dot{M}$ and with Hβ luminosity.

To compare our results with those of Johnstone *et al.* we have applied an evolutionary stellar population synthesis technique to compute how the 4000 Å break and the Mg_2 index change if there is ongoing star formation. We would expect the Mg_2 index to reflect ongoing star formation with a normal IMF because it is sensitive to effective temperature. Our population synthesis model is similar to that used by Bruzual (1983); stellar evolutionary tracks for dwarfs and giants of half solar abundance were computed from data given by VandenBerg (1985) and Tinsley & Gunn (1976). We used the library of stellar spectra, published by Pickles (1985), to produce synthetic spectra for a given IMF and star formation history which we superimpose on the spectrum of a normal giant elliptical with $Mg_2 = 0.34$ and $D_{4000} = 2.4$. Further details of the models may be found in Aragón, Gorgas & Rego (1987). Fig. 6 shows the results for different IMF's, a Miller & Scalo (1979) function, and power laws of slope $x = 0$, 1 and 2 [$dN(m)/dm \propto m^{-(1+x)}$]; in all cases we truncate the IMF at masses below $0.05\,M_\odot$. We assume that star formation occurs at a constant rate and we present results for two durations of star formation, 5 and 10 Gyr. The diagram shows the change in D_{4000} against the change in Mg_2 as a function of the fraction, f_V, of the total V light that comes from the stars formed from the accreting gas. This fraction is related to the star formation rate by

$$SFR = \frac{f_V L_V (M/L_V)_{AP}}{t},$$

where L_V is the V luminosity of the cD galaxy, $(M/L_V)_{AP}$ is the mass-to-light ratio in the V-band of the accretion population, which is given by the models, and t is the time over which the stars have been forming. For example, for the Miller–Scalo IMF, the models give $(M/L_V)_{AP} = 2.4$ and 1.6 for ages of 5 and 10 Gyr, respectively.

The results of Fig. 4 show that the galaxies with high $\dot{M}$ deviate by less than $\Delta Mg_2 \sim -0.03$ from the Mg_2–σ_0 relation of normal ellipticals. Fig. 6, shows that $\Delta Mg_2 < -0.03$ corresponds to $f_V < 0.1$ in all the models, and to a change of $\lesssim -0.3$ in D_{4000}. Johnstone *et al.* find $D_{4000} \sim 2$ for most of their galaxies with $\dot{M} \sim 100\,M_\odot\ \mathrm{yr}^{-1}$, which is lower than the typical value of $D_{4000} \approx 2.4$ in the nuclear regions of luminous ellipticals. Thus, the limits on star-formation deduced from our constraints on Mg_2 may be just compatible with the low values of D_{4000} reported by Johnstone *et al.* if stars are forming with a normal IMF. We note that the correlations found by Johnstone *et al.* of D_{4000} against $\dot{M}$ and of D_{4000} against Hβ luminosity rely heavily on the extremely low value of $D_{4000} \sim 1$ observed for PKS0745-191 (for which $\dot{M} \sim 1000$

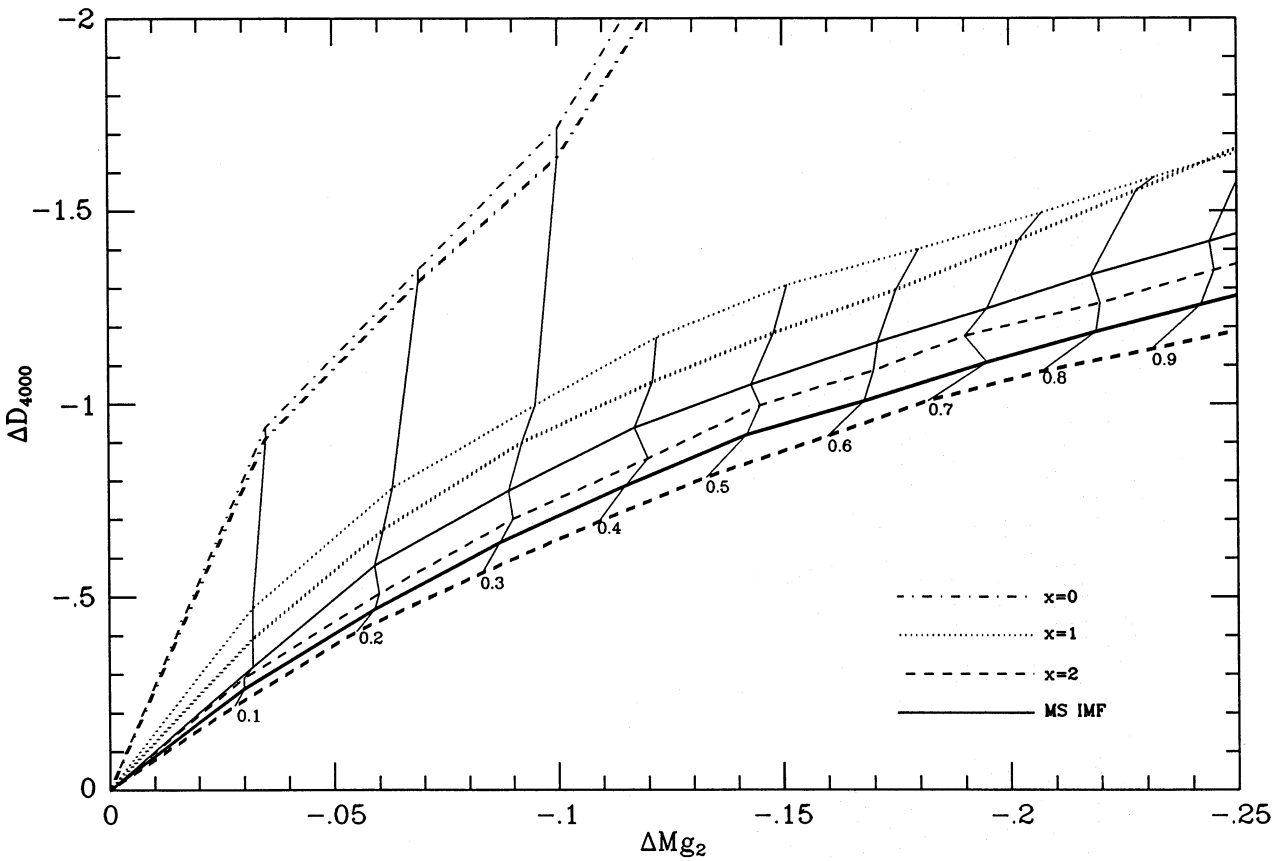

Figure 6. Population synthesis models of the change in the Mg_2 index and the 4000 Å break, D_{4000}, in a luminous elliptical galaxy in which cooling gas forms stars at a constant rate (see the text for details). Results are presented for several values of the slope, x, of the IMF and for a Miller–Scalo IMF, as indicated in the figure. Models in which star formation has been taking place for the last 5 and 10 Gyr are shown by the thin and thick lines, respectively. The lines joining these predictions correspond to a fixed fraction f_V (indicated by the numbers) of the V light that comes from the accretion population.

$M_\odot$ yr^{-1}); if this value of D_{4000} is correct, then our analysis predicts a large change in Mg_2 of ~ 0.25 mag unless the IMF is skewed towards massive stars ($x \sim 0$, Fig. 6). It is important to obtain further data on this, and other cooling flow galaxies, to check the accuracy of Johnstone *et al.*'s measurements and to check for radial gradients in D_{4000}. Note that $\dot{M}$ and D_{4000} in Johnstone *et al.*'s sample are highly correlated with the redshift of the galaxy and so radial gradients in D_{4000} could lead to an aperture effect as described above for Mg_2.

Our limit of $f_V \lesssim 0.1$ translates to global star formation rates of $\lesssim 6$ and $\lesssim 2 M_\odot$ yr^{-1} for $t = 5$ and $t = 10$ Gyr, respectively assuming $M_V \sim -23$ for the cD galaxy. This agrees with the conclusions of Johnstone *et al.* and O'Connell & McNamara (1987) that only a small fraction of the cooling gas could be forming stars with a normal IMF, the precise fraction depending on the form of the gas deposition profile. If most of the cooling gas forms stars with a power law like IMF, then our population synthesis models imply that the IMF must have an upper mass cut-off at $\lesssim 0.5 M_\odot$ (*cf.* O'Connell & McNamara 1987, who reach a similar conclusion).

4 LINE-STRENGTH GRADIENTS

Line-strength indices for the AAT sample are listed in Appendix B; the numbers in brackets give the corrections to reduce our measurements to zero velocity dispersion and the column labelled N_c gives the number of photons in each spectrum in units of 10^6. Since the Mg_2 index is the most accurately measured line-strength index, we discuss Mg_2 gradients first in Section 4.1. In Section 4.2 we investigate whether Mg_2 gradients correlate with any other observables, such as total luminosity, central velocity dispersion or surface brightness. In Section 4.3 we investigate gradients in other line-indices and compare our results with line-strength measures of galactic globular clusters.

4.1 Mg_2 gradients

4.1.1 Ellipticals and lenticulars

Mg_2 gradients in early-type galaxies have been discussed by Faber (1977). She compared the variation in Mg_2 with $\log[r/R(0)]$* in four galaxies and concluded that the gradients had similar slopes. Results were presented for only one elliptical (NGC 4472), two S0s (NGC 3115 and NGC 7332) and the nuclear bulge of M31, but were quoted as representative of a larger sample of eight early-type galaxies.

A similar comparison is shown in Fig. 7 for the ellipticals and S0s in our sample. Instead of using $R(0)$, we plot the Mg_2 values along the major axis of each galaxy against $\log(r/r_e)$, where r_e is de Vaucouleurs' effective radius listed in the RC2 (see Table 6). We assigned a luminosity weighted radius r to each value of Mg_2,

$$r = \frac{\int \mu(s)\, s\, ds}{\int \mu(s)\, ds}, \quad \mu(s) \propto 10^{bs}, \tag{5}$$

where the appropriate value of b for each scan was determined from the photon counts in it and in neighbouring scans. In Fig. 7 we have averaged the Mg_2 values on either side of each galaxy. For IC 4296 and NGC 4472 we have measured the Mg_3 index and converted to Mg_2 using equation (3). For each galaxy we show error bars appropriate to the inner and outermost points (see Appendix A). In Fig. 7 we compare Faber's observations (triangles) with our results for NGC 4472, which is the only galaxy in our sample for which an Mg_2 gradient has been published. The agreement is extremely good.

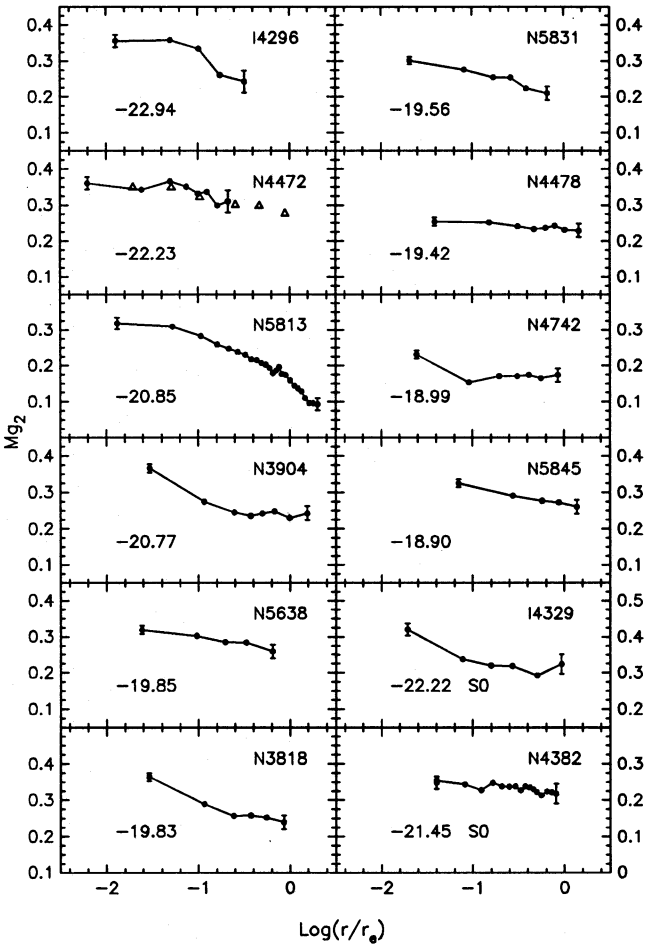

Figure 7. Major axis Mg_2 gradients in 12 early-type galaxies. We have plotted Mg_2 versus $\log(r/r_e)$, where r_e is de Vaucouleurs' effective radius as listed in the RC2. For each galaxy we give the absolute magnitude in the B_T system assuming a Hubble constant of $H_0 = 50$ km s^{-1} Mpc^{-1}. The error bars give an estimate of the errors for the inner and outer points as discussed in Appendix A. The triangles show Faber's (1977) measurements of Mg_2 in NGC 4472.

Fig. 7 shows that there are large variations in the Mg_2 gradients from galaxy to galaxy. Several galaxies show steep gradients (e.g. NGC 3818, 3904, 5813), while the gradients in others are weak (e.g. NGC 4382, 4478). Our results also indicate that the gradients flatten off in the outer parts of some galaxies (e.g. NGC 3904, 4742). Our error estimates strongly suggest that the flattening of the Mg_2 gradients seen in some galaxies is real. These results clearly do not support Faber's conclusion that all early-type galaxies show similar Mg_2 gradients.

We have estimated the slopes of the Mg_2 profiles shown in

* $R(0) = D(0)/2$, where $D(0)$ is the corrected face-on diameter listed in the *Second Reference Catalogue of Bright Galaxies* (de Vaucouleurs, de Vaucouleurs & Corwin 1976, hereafter RC2).

Table 6. Observational parameters for early-type galaxies.

Galaxy	M_B (a)	r_e (b)	μ_e (c)	$\log\bar{\sigma}$ (d)	$\log\sigma_o$ (e)	ε (f)	$V_m/\bar{\sigma}$ (g)	S_σ (h)	$\overline{Mg_2}$ (i)	Mg_2^F (j)	S_{Mg_2}	ΔS_{Mg_2}
N 3136	−20.97	25	3.20	–	2.377	0.32	–	–	–	0.298	–	–
N 3605	−18.16	17	1.39	1.954	1.959	0.41	0.58	+0.001	–	0.244	–	–
N 3608	−19.32	27	1.60	–	2.258	0.19	–	–	–	0.345	–	–
N 3818	−19.83	19	1.63	2.179	2.292	0.32	0.75	−0.189	0.312	0.345	−0.083	0.012
N 3904	−20.77	19	3.47	2.307	2.294	0.26	0.31	+0.017	0.296	0.339	−0.084	0.016
N 3923	−21.62	30	3.04	–	2.396	0.35	–	–	–	0.332	–	–
N 3962	−20.98	29	2.01	–	2.369	0.09	–	–	–	0.312	–	–
N 4382	−21.45	60	1.68	2.310	2.246	0.26	0.39	+0.081	–	–	−0.025	0.005
N 4458	−18.65	21	1.04	–	2.000	0.05	–	–	–	0.255	–	–
N 4472	−22.23	99	1.27	2.408	2.491	0.18	0.17	−0.143	0.341	0.356	−0.042	0.007
N 4476	−18.40	15	1.62	–	1.875	0.32	–	–	–	0.153	–	–
N 4478	−19.42	15	4.16	2.152	2.161	0.15	0.44	−0.028	0.249	0.252	−0.014	0.005
N 4489	−18.68	22	0.98	–	1.724	0.05	–	–	–	0.229	–	–
N 4742	−18.99	23	1.19	1.826	2.041	0.34	1.26	−0.241	0.188	0.209	−0.030	0.016
N 5638	−19.85	24	1.00	2.182	2.188	0.09	0.41	−0.073	0.300	0.312	−0.040	0.006
N 5813	−20.85	44	0.77	2.340	2.352	0.25	0.04	+0.043	0.286	0.316	−0.089	0.006
N 5831	−19.56	27	0.62	2.170	2.182	0.09	0.18	−0.065	0.274	0.292	−0.060	0.007
N 5845	−18.90	8	3.86	2.288	2.420	0.35	0.65	−0.245	0.306	0.316	−0.049	0.004
I 4296	−22.94	48	0.82	2.464	2.477	0.10	0.22	−0.056	0.321	0.360	−0.087	0.030
I 4329	−22.22	31	0.66	2.487	2.481	0.51	0.12	+0.046	0.347	0.400	−0.062	0.019
0559-40	–	25	–	2.452	2.444	0.31	–	−0.008	0.302	0.318	−0.051	0.019
2354-35	–	80	–	2.511	2.471	0.28	–	+0.130	0.261	0.288	−0.021	0.006
Ser40/6	–	71	–	2.563	2.515	0.36	–	–	0.269	0.291	–	–
N 3115	−19.74	34	4.98	2.265	2.391	0.57	1.06	–	–	0.330	−0.084	0.009
N 7332	−20.03	17	4.15	–	2.188	0.69	–	–	–	–	−0.062	0.000
	0.37		0.18	−0.47	−0.50	−0.17	0.37	−0.15	−0.35	−0.56		
	(14)		(14)	(13)	(14)	(14)	(13)	(12)	(11)	(12)		

Fig. 7 using least-squares fits. We have restricted the fits to $r < r_e$. This provides an objective measure of the Mg_2 gradients and, for most galaxies, a power law is a reasonable approximation over this range. However, the effects of seeing may lead to underestimates of the Mg_2 gradients, particularly in galaxies with small angular diameters (e.g. NGC 5845 for which $r_e \simeq 8$ arcsec). The gradients and formal errors are listed in the last two columns of Table 6. The mean of the Mg_2 gradients for the elliptical galaxies listed in Table 6 is

$$Mg_2 = -(0.058 \pm 0.027)\log(r/r_e) + \text{constant}, \quad (6)$$

where the error gives the standard deviation about the mean. Equation (6) agrees with the mean Mg_2 gradient for six early-type galaxies studied by Couture & Hardy (1988). The two luminous S0 galaxies in our sample have Mg_2 gradients compatible with equation (6) (Fig. 7, Table 6).

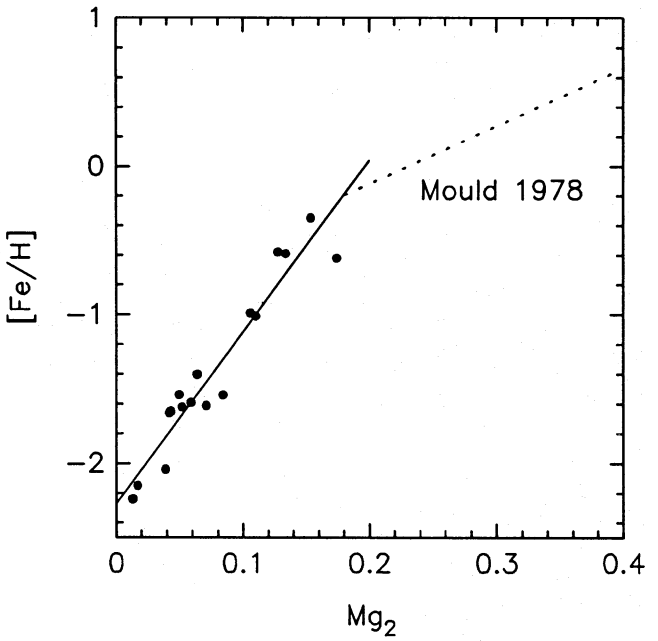

Figure 8. Mg_2 values for galactic globular clusters (from BFGK) plotted against estimates of [Fe/H] from Zinn & West (1984). The solid line shows the least-squares fit of equation (7). The dotted line shows a calibration (equation 8) of the Mg_2 index at high metallicities for a 13 Gyr stellar population (Mould 1978).

It is impossible to convert variations in the strength of a single feature into true metallicity gradients. To calibrate abundance variations in ellipticals will require comparisons of spectral synthesis models with high quality spectroscopy over a wide wavelength range. This has been attempted for the nuclei of ellipticals, but there are still ambiguities in disentangling the effects of age and metallicity (see Burstein 1985 and Pickles 1987, for recent reviews). However, if we assume that elliptical galaxies have the same ages as galactic globular clusters, we can calibrate the Mg_2 index at low metallicities using the line-indices for galactic globulars in BFGK (e.g. Burstein 1979). In Fig. 8 we have plotted BFGK's Mg_2 values for 17 galactic globular clusters against estimates of [Fe/H] from Zinn & West (1984). A least squares fit to these points gives

$$[\text{Fe/H}] = 11.551\ Mg_2 - 2.274. \quad (7)$$

However, this relationship is only valid for the range of Mg_2

spanned by galactic globular clusters (i.e. $Mg_2 \leq 0.17$), so it might apply at best to the outer regions of some elliptical galaxies. To estimate the metallicities of typical elliptical nuclei a different approach is needed. The dotted line in Fig. 8 shows Mould's (1978) theoretical computation (as recalibrated by Terlevich *et al.* 1981) for the relation between the Mg_2 index and [Fe/H] for an old (13 Gyr) stellar population over the range $-0.5 \lesssim [Fe/H] \lesssim 0.3$

$$[Fe/H] \approx 3.9\, Mg_2 - 0.9. \quad (8)$$

If we assume that this calibration is correct, then the mean metallicity gradient for our sample of early-type galaxies is

$$\frac{d[Fe/H]}{d \log(r/r_e)} \approx -(0.22 \pm 0.10). \quad (9)$$

This result implies relatively modest metallicity gradients in most elliptical galaxies, from abundances of ~ 2–3 times solar in the nuclei of luminous ellipticals to roughly solar abundances at $r \sim r_e$. This agrees with Cohen's (1986) conclusions based on her observations of weak colour gradients in three Virgo elliptical galaxies. In Section 4.3 we present additional evidence for relatively weak abundance gradients in ellipticals from a comparison of Fe line-strength indices with those measured in galactic globular clusters.

The mean abundance gradient implied by equation (9) is similar to the abundance gradients of $d \log Z/d \log r \approx -0.35$ predicted by Larson's (1974, 1975) dissipative collapse models for the formation of ellipticals. In Larson's models, the shape of the metallicity gradients is fixed by the star-formation rate; steep metallicity gradients are produced if the star-formation rate is slower than the time-scale for gas to sink into the central regions, but models with a high star-formation rate during the early phases of collapse produce gradients which flatten off beyond ~ 1 kpc from the centre. Clearly, in the extreme case of purely dissipationless collapse with a constant IMF (ignoring stellar mass loss etc., e.g. Gott 1973, 1975) one would not expect any metallicity gradient.

Larson's spherical collapse models are almost certainly an oversimplified description of the formation of ellipticals. If galaxies formed by the gravitational amplification of small amplitude Gaussian density fluctuations, we would expect a collapsing protocloud to be highly inhomogeneous (e.g. Frenk *et al.* 1985; Efstathiou 1990). The main body of an elliptical galaxy would then form by the merging of subsystems in which some star formation has already taken place. If the subunits are predominantly stellar, metallicity gradients might be weakened by successive merging, producing a galaxy with weak abundance gradients. Alternatively, metallicity gradients might be created by star formation during the merging of gas-rich subsystems. The large variation in the shapes of the line-strength profiles seen in Fig. 7 may indicate that these processes operate to varying degrees in different ellipticals. In this type of model, it would be surprising if all ellipticals had exactly the same abundance gradients.

We have measured Mg_2 gradients along the major and minor axes of the three ellipticals observed in Run 1 (see Appendix B). In each case, there is no significant difference between the major- and minor-axis gradients in Mg_2 or of the other line indices. These results suggest that the contours of fixed metallicity have similar flattening to the isophotes, though since none of these galaxies is very flat, we cannot differentiate between some of the theoretical predictions that have appeared in the literature (e.g. Larson 1975; Carlberg 1984).

4.1.2 *Line-strength gradients in cD galaxies*

The Mg_2 gradients for the three cD galaxies of Run 5 are shown in Fig. 9. Sersic 40/6 is a dumb-bell galaxy, so we have not averaged the Mg_2 measurements from either side of the galaxy. Fig. 9 shows that these galaxies also possess Mg_2 gradients. The slopes of the Mg_2 gradients for 0559-40 and PKS2354-35 are listed in Table 6. These galaxies have shallower gradients than the mean of ellipticals (equation 6). However, since ellipticals show such a large scatter about the mean relation, more data are required to test whether the line-strength gradients in cD's are systematically shallower than those of normal ellipticals. We note that the metallicity gradients in cD galaxies should be shallower than in normal luminous ellipticals if cD's formed by prolific merging of ellipticals during the formation of rich clusters of galaxies (e.g. Hausman & Ostriker 1978; Merritt 1985).

The estimated cooling time of the X-ray gas in the core of Sersic 40/6 is longer than a Hubble time, $t_{cool} \sim 2.5 \pm 0.8 \times 10^{10}$ yr, whereas PKS2354-35 shows a mass-deposition rate of $\dot{M} \gtrsim 100 M_\odot$ yr^{-1} (Arnaud & Fabian, private communication) (Arnaud & Fabian quote a central cooling time for 0559-40 of 41×10^{10} yr). However, Fig. 9 shows that there is no obvious difference in the Mg_2 gradients in these galaxies. In Section 3.2 we showed that PKS2354-35 has nuclear Hβ emission. The lower panels in Fig. 9 show Hβ profiles in these galaxies, and it can be seen that the Hβ emission in PKS2354-35 is confined to the central regions ($\lesssim 8$ arcsec). Cooling flow galaxies often show emission concentrated in their central regions (Cowie *et al.* 1983).

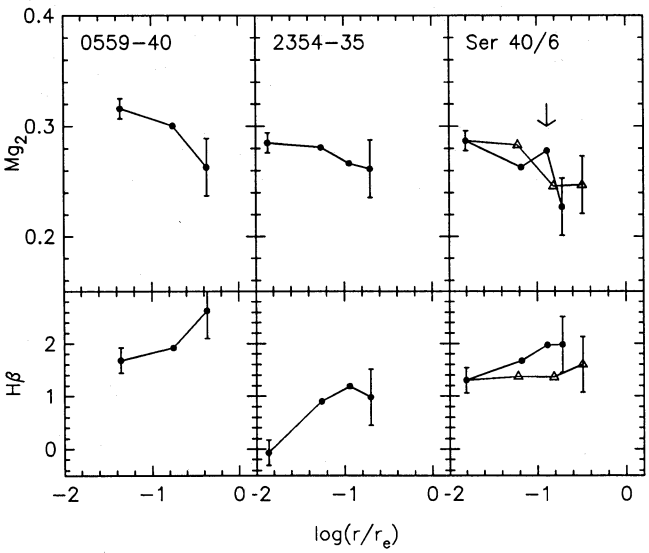

Figure 9. The upper panel shows Mg_2 gradients along the major axes in the three cD galaxies of Run 5. Sersic 40/6 is a dumb-bell galaxy, so we have plotted points on either side of the centre of the more luminous component using different symbols. The position of the secondary nucleus is indicated by the arrow. The lower panel shows the profiles for the Hβ line index.

4.2 Correlations between Mg_2 gradients and other parameters

The results presented in Section 4.1 show that the Mg_2 gradients in ellipticals vary considerably from galaxy to galaxy. It is clearly important to establish whether these variations reflect irregularities during galaxy formation, or whether they are tightly correlated with other parameters of the sample. We have therefore applied the Spearman rank correlation test to check for correlations between Mg_2 gradients and various parameter listed in Table 6. This Table gives the following parameters (where available) for each galaxy: (a) M_B is the blue absolute magnitude computed from the B_T magnitude listed in the RC2 assuming a uniform Hubble flow and a Hubble constant $H_0 = 50$ km s^{-1} Mpc^{-1} (see Davies *et al.* 1983); (b) r_e is the effective radius in arcsec; (c) μ_e is the mean surface-brightness interior to r_e in units of $10^9 L_\odot$ kpc^{-2}; (d) $\log \bar{\sigma}$ is the mean velocity dispersion within $r_e/2$; (e) $\log \sigma_0$ is the central velocity dispersion from the references listed in Table 1; (f) ε is the ellipticity listed in Davies *et al.*, the RC2 and Carter *et al.* (1985); (g) $V_m/\bar{\sigma}$, where V_m is the maximum rotational velocity as defined by Davies *et al.*; (h) $S_\sigma = d\log(\sigma)/d\log(r/r_e)$ is a measure of the slope of the velocity dispersion profile and has been calculated by least-square fits for measurements with $r < r_e/2$ from the sources listed in Table 1; (i) $\overline{Mg_2}$ is a global measure of Mg_2 which we estimated by adding together all spectra within $r_e/2$ (except for NGC 4472 for which our spectra extend only to $r_e/4$); (j) Mg_2^F is a measure of Mg_2 within an aperture of similar dimensions to the 1.4×4 arcsec used by the Lick group. The last two columns of Table 6 list the Mg_2 gradients and formal errors in the slopes. We also give parameters for two S0 galaxies (NGC 3115, 7332) with Mg_2 gradient measured by Faber (1977).

The rank correlation coefficients, r_s, between the Mg_2 gradients and these parameters (except for r_e) are listed in the penultimate row of Table 6. The numbers in brackets give the number of galaxies used to test each correlation; we have excluded the three cD galaxies in these comparisons. The strongest correlations are with central velocity dispersion and central Mg_2 and are significant at about the 95 per cent level (see, e.g. Press *et al.* 1986). These correlations are in the sense that galaxies with high central velocity dispersions, or high central values of Mg_2, exhibit steep line-strength gradients. Burstein (1979) also noted a tendency for galaxies with high central values of $(Mg)_0$ to have steeper nuclear gradients.

Fig. 10(a) and (b) show the correlations of Mg_2 gradients with σ_0 and central Mg_2. These correlations are not independent because σ_0 and central Mg_2 are tightly correlated (equation 4). The two cD galaxies are plotted as triangles in Fig. 10(a) and (b). Including the cD galaxies clearly weakens the correlations, especially the one between S_{Mg_2} and σ_0. Further data are required to decide whether these correlations are real, and whether cD galaxies deviate from them. However, it is clear from Fig. 10(a) and (b) that even if further data show that these correlations are statistically significant, there is considerable scatter in both relations.

None of the other correlations summarized in Table 6 are significant. For example, the correlation between Mg_2 gradients and absolute magnitude (plotted in Fig. 10c) is significant at less than the 80 per cent level. Davies & Sadler (1987) presented tentative evidence that luminous ellipticals have shallower Mg_2 gradients than fainter ones, but this trend is not supported by our larger sample.

The results of Section 4.1 provide strong evidence that elliptical galaxies have undergone different star-formation histories. Evidently, ellipticals are not a uniform class of galaxies as has often been thought; either strong or weak metallicity gradients can result from physical processes in proto-elliptical galaxies. The analysis of this section shows that these physical processes are not strongly correlated with fundamental parameters of ellipticals, though there may be a tendency for more tightly bound (i.e. high σ_0) systems to produce stronger lined galaxies with steeper abundance gradients. The lack of any clear correlations indicates that there must have been substantial stochastic variations in the way that stars formed within proto-ellipticals. This would seem inevitable if ellipticals formed by the mergers of gas-rich subsystems are suggested in Section 4.1.

4.3 Gradients in other line-strength indices

In a previous paper (Efstathiou & Gorgas 1985) we described line-strength gradients out to large radii measured from high signal-to-noise spectra of NGC 5813. In fig. 3 of that paper we compared our line-strength measurements with indices measured by BFGK for galactic globular

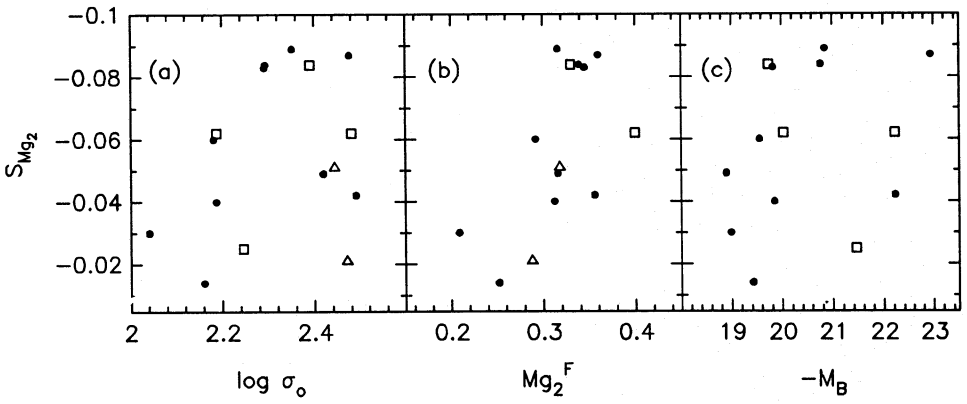

Figure 10. Plots of the slope of the Mg_2 gradient, S_{Mg_2}, versus central velocity dispersion (a), central Mg_2 (b) and absolute magnitude (c) for the galaxies listed in Table 6. The filled circles show results for ellipticals, open squares for S0s and the open triangles for cD galaxies.

clusters and for the nuclei of elliptical galaxies and concluded that the line-strengths in the outer regions of NGC 5813 match continuously with those of metal rich galactic globular clusters. The Hβ index in NGC 5813 was found to be nearly constant with radius outside the nuclear regions and we detected steep radial gradients in the iron lines. When we plotted the Fe and Hβ indices against Mg_2, we found that the line-strengths in NGC 5813 obeyed a different set of relations from those determined by BFGK for the nuclei of elliptical galaxies (*cf.* Fig. 3). This suggests that the stellar populations in elliptical galaxies do not represent a simple one-parameter family, and may indicate radial variations in the mean age of the stellar population as well as variations in metallicity (e.g. Pickles 1987).

These results clearly need to be confirmed by other measurements. However, the exposures for the other galaxies in our sample are much shorter than for NGC 5813, consequently we cannot measure accurate line-strengths to such large radii ($\sim 2r_e$). Nevertheless, we can measure gradients in Fe and Hβ out to ~ 0.5–$1r_e$.

We have estimated gradients in other indices following the procedure described in Section 4.1 for Mg_2 gradients. The mean line-strength gradients for the ellipticals and S0s in our sample are

$$d\,\mathrm{Mg_1}/d\,\log(r/r_e) = -(0.035 \pm 0.025)$$

$$d\,\mathrm{Mg}b/d\,\log(r/r_e) = -(0.61 \pm 0.42)$$

$$d\,\mathrm{H}\beta/d\,\log(r/r_e) = -(0.03 \pm 0.21)$$

$$d\,\mathrm{Fe52}/d\,\log(r/r_e) = -(0.49 \pm 0.31)$$

$$d\,\mathrm{Fe53}/d\,\log(r/r_e) = -(0.66 \pm 0.38)$$

$$d\langle\mathrm{Fe}\rangle/d\,\log(r/r_e) = -(0.57 \pm 0.34),$$

where the errors represent the standard deviations about the mean. NGC 4742 was excluded in determining the mean Hβ gradient, since its central Hβ index is anomalously large (3.8 Å). As with the Mg_2 gradients described in Section 4.1, the gradients in the other features also vary substantially from galaxy to galaxy.

In Fig. 11 we show the line-strengths in the inner and outer regions of the elliptical galaxies from Run 3 plotted against Mg_2. We have averaged the results in the outer parts of each galaxy (typically between $0.5r_e$ to r_e) which are plotted as the crosses in Fig. 11, where the extent of the cross in each direction gives the standard deviation of the averaged line-strength index. These crosses are connected to the nuclear line-strengths to give an impression of the gradients within each galaxy. Hβ is found to be nearly constant with radius, with the exception of NGC 4742 in which Hβ falls from the extremely high central values, to more normal

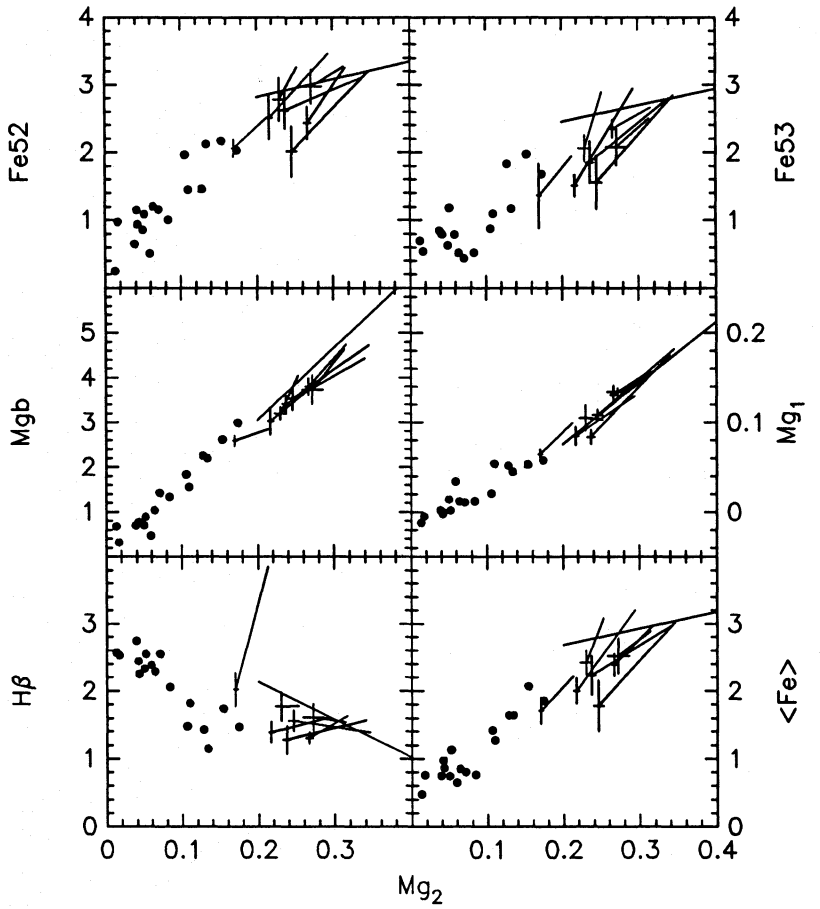

Figure 11. A comparison of the line-strengths of galactic globular clusters from BFGK (filled circles) with those for the ellipticals of Run 3. The crosses show line-strengths in the outer parts of each galaxy (typically $r \sim 0.5 - 1r_e$) and their extent in each direction gives the rms error in each line index. The crosses have been connected to the nuclear line-strengths by straight lines to show the gradients within each galaxy. The solid lines show the mean relations deduced by BFGK for the nuclei of ellipticals.

values at larger radii. For most of the galaxies, the Fe line-strengths fall quite steeply.

Fig. 11 shows the same general trends that we found in our analysis of NGC 5813. In Fig. 11, Hβ in the outer parts of elliptical galaxies is lower than would have been inferred from the relation obeyed by elliptical nuclei. Although the Fe indices show little variation amongst the nuclei of ellipticals, they vary more strongly within a particular galaxy. We conclude that the stellar populations at large radii in ellipticals do not obey the same Mg_2–Hβ and Mg_2–Fe relationships as do the nuclei of elliptical galaxies.

For NGC 5813, we found that the line-indices at $\gtrsim r_e$ matched continuously with those of metal-rich galactic globular clusters. Although the results for the ellipticals plotted in Fig. 11 do not extend to such large radii, there seems to be continuity with the line-indices of galactic globular clusters, suggesting that the typical elliptical galaxies at ~ 0.5–$1 r_e$ have slightly higher metal abundance (i.e. about solar) than the most metal rich globular cluster plotted in the figure. This is consistent with our estimate of the radial abundance variations based on the Mg_2 gradients and Mould's (1978) calibration (Fig. 8).

5 CONCUSIONS

Our results have shown the following.

(i) Our nuclear line-strength measurements in ellipticals follow the relations found by BFGK. We confirm that low-luminosity ellipticals have higher Hβ indices than metal-rich galactic globular clusters with similar values of Mg_2.

(ii) The metallic line-strengths in the clusters of brightest cluster galaxies are indistinguishable from those of normal ellipticals with similar central velocity dispersions. However, some cD galaxies at the centres of prolific cooling flows show Hβ emission. Our population synthesis models show that only a small fraction of the cooling gas could be forming stars with a normal IMF, otherwise the central Mg_2 indices in these galaxies would be systematically lower than in normal luminous ellipticals or cD's without cooling flows.

(iii) The line-strength gradients in early-type galaxies are highly variable. These variations do not correlate strongly with other parameters, though we find some evidence that galaxies with high central velocity dispersions and high central line-strengths tend to have steeper gradients. The mean Mg_2 gradient for our sample, and Mould's (1978) theoretical calibration of the Mg_2 index, suggests that the metallicity gradients in ellipticals are relatively weak. Our results suggest that in a typical luminous elliptical galaxy, the metallicity drops from about 2–3 times solar abundance in the nuclear regions, to about solar abundance at $r \sim 0.5$–$1 r_e$.

(iv) The line-strength gradients in two, bulge-dominated, lenticular galaxies are similar to those of normal ellipticals. We have measured Mg_2 gradients for three cD galaxies in our sample and find that they have slightly weaker gradients than the mean for normal ellipticals.

(v) The Mg, Fe and Hβ line-strengths in the outer parts of ellipticals ($r \sim r_e$) are similar to those of metal rich galactic globular clusters, suggesting roughly solar abundances at these radii.

(vi) Our results support our earlier conclusions from an analysis of NGC 5813 (Efstathiou & Gorgas 1985) that the line-strengths within elliptical galaxies follow a different set of relations from those obeyed by the nuclei of ellipticals. The Hβ index is approximately constant with increasing radius (decreasing Mg_2), whereas in the nuclei of ellipticals the Hβ index rises as Mg_2 decreases. In most ellipticals, the Fe indices decrease with radius more rapidly than implied by the Fe–Mg_2 relations followed by elliptical nuclei. These deviations from a set of one parameter relations may be indicative of variations in both age and metallicity in the stellar populations of ellipticals (e.g. Pickles 1987).

Point (iii) is the most significant result to emerge from this study for it indicates that elliptical galaxies have experienced different star-formation histories. This would seem natural if ellipticals formed by the merging of subunits of variable gas-to-star ratio as various authors have suggested for other reasons (e.g. Norman & Silk 1980). Point (vi) has interesting implications for our understanding of the stellar populations in elliptical galaxies. It is important to extend these observations and to begin to construct population synthesis models of the outer parts of elliptical galaxies.

ACKNOWLEDGMENTS

JG would like to thank the Institute of Astronomy, Cambridge, and the Department of Astrophysics, Oxford, for their hospitality. He acknowledges support by the Spanish Fondo Nacional para el Desarrollo de la Investigación Científica (Project PB85-60). GE would like to thank his observing collaborators; this project would have been impossible without their effects. We thank the British Council for providing travel support.

REFERENCES

Abell, G. O., Corwin, H. G. & Olowin, R., 1989. *Astrophys. J. Suppl.*, **70**, 1.
Aragón, A., Gorgas, J. & Rego, M., 1987. *Astr. Astrophys.*, **185**, 97.
Bosma, A., Smith, R. M. & Wellington, K. J., 1985. *Mon. Not. R. astr. Soc.*, **212**, 301.
Bruzual, G., 1983. *Astrophys. J.*, **273**, 105.
Burstein, D., 1979. *Astrophys. J.*, **232**, 74.
Burstein, D., 1985. *Publs astr. Soc. Pacif.*, **97**, 89.
Burstein, D., Faber, S. M., Gaskell, C. M. & Krumm, N., 1984. *Astrophys. J.*, **287**, 586 (BFGK).
Carlberg, R. G., 1984. *Astrophys. J.*, **286**, 403.
Carter, D., Inglis, I., Ellis, R. S., Efstathiou, G. & Godwin, J., 1985. *Mon. Not. R. astr. Soc.*, **212**, 471.
Cohen, J. G., 1986. *Astr. J.*, **92**, 1039.
Couture, J. & Hardy, E., 1988. *Astr. J.*, **96**, 867.
Cowie, L. L., Hu, E. M., Jenkins, E. B. & York, D. G., 1983. *Astrophys. J.*, **272**, 29.
Davies, R. L. & Sadler, E. M., 1987. *Structure and Dynamics of Elliptical Galaxies, IAU Symp. No. 127*, p. 441, ed. de Zeeuw, T., Reidel, Dordrecht.
Davies, R. L., Efstathiou, G., Fall, S. M., Illingworth, G. & Schechter, P. L., 1983. *Astrophys. J.*, **266**, 41.
Davies, R. L., Burstein, D., Dressler, A., Faber, S. M., Lynden-Bell, D., Terlevich, R. J. & Wegner, G., 1987. *Astrophys. J. Suppl.*, **64**, 581.
de Vaucouleurs, G., 1961. *Astrophys. J. Suppl.*, **5**, 233.
de Vaucouleurs, G., de Vaucouleurs, A. & Corwin, H. G., 1976. *Second Reference Catalogue of Bright Galaxies*, University of Texas, Austin (RC2).
Dressler, A., 1984. *Ann. Rev. Astr. Astrophys.*, **22**, 185.

Edge, A., 1988. *PhD thesis,* University of Leicester.
Efstathiou, G., 1990. In: *Dynamics and Interactions of Galaxies,* ed. Weilen, R., Springer-Verlag, in press.
Efstathiou, G. & Gorgas, J., 1985. *Mon. Not. R. astr. Soc.,* **215,** 37P.
Efstathiou, G., Ellis, R. S. & Carter, D., 1980. *Mon. Not. R. astr. Soc.,* **193,** 931.
Efstathiou, G., Ellis, R. S. & Carter, D., 1982. *Mon. Not. R. astr. Soc.,* **201,** 975.
Faber, S. M., 1977. In: *The Evolution of Galaxies and Stellar Populations,* p. 157, eds Tinsley, B. M. & Larson, R. B., Yale University Observatory, New Haven.
Faber, S. M., 1983. *Highlights of Astronomy,* **6,** 165.
Faber, S. M., Burstein, D. & Dressler, A., 1977. *Astr. J.,* **82,** 941.
Fabian, A. C., Ku, W. H.-M., Malin, D. F., Mushotzky, R. F., Nulsen, P. E. J. & Stewart, G. C., 1981. *Mon. Not. R. astr. Soc.,* **196,** 35P.
Frenk, C. S., White, S. D. M., Efstathiou, G. & Davis, M., 1985. *Nature,* **317,** 595.
Gorgas, J., 1987. *PhD thesis,* Universidad Complutense, Madrid.
Gorgas, J. & Efstathiou, G., 1987. *Structure and Dynamics of Elliptical Galaxies, IAU Symp. No. 127,* p. 189, ed. de Zeeuw, T., Reidel, Dordrecht.
Gott, J. R., 1973. *Astrophys. J.,* **186,** 481.
Gott, J. R., 1975. *Astrophys. J.,* **201,** 296.
Gunn, J. E., Stryker, L. L. & Tinsley, B. M., 1981. *Astrophys. J.,* **249,** 48.
Hausman, M. A. & Ostriker, J. P., 1978. *Astrophys. J.,* **224,** 320.
Heckman, T. M., 1981. *Astrophys. J.,* **250,** L59.
Jenkins, C. R., 1987. *Mon. Not. R. astr. Soc.,* **226,** 341.
Jenkins, C. R. & Scheuer, P. A. G., 1980. *Mon. Not. R. astr. Soc.,* **192,** 597.
Johnstone, R. M., Fabian, A. C. & Nulsen, P. E. J., 1987. *Mon. Not. R. astr. Soc.,* **224,** 75.
Larson, R. B., 1974. *Mon. Not. R. astr. Soc.,* **166,** 585.
Larson, R. B., 1975. *Mon. Not. R. astr. Soc.,* **173,** 671.
Merrit, D., 1985. *Astrophys. J.,* **289,** 18.
Miller, G. E. & Scalo, J. M., 1979. *Astrophys. J. Suppl.,* **41,** 513.
Mould, J. R., 1978. *Astrophys. J.,* **220,** 434.
Norman, C. A. & Silk, J., 1980. *Astrophys. J.,* **238,** 158.
O'Connell, R. W., 1980. *Astrophys. J.,* **236,** 430.
O'Connell, R. W. & McNamara, B. R., 1987. In: *Cooling Flows in Clusters and Galaxies,* NATO ASI, p. 103, ed. Fabian, A. C., Kluwer, Dordrecht.
Oke, J. B., 1974. *Astrophys. J. Suppl.,* **27,** 21.
Ostriker, J. P., 1977. In: *The Evolution of Galaxies and Stellar Populations,* p. 369, eds Tinsley, B. M. & Larson, R. B., Yale University Observatory, New Haven.
Ostriker, J. P., 1980. *Comm. Astrophys.,* **8,** 177.
Pickles, A. J., 1985. *Astrophys. J.,* **296,** 340.
Pickles, A. J., 1987. *Structure and Dynamics of Elliptical Galaxies, IAU Symp. No. 127,* p. 203, ed. de Zeeuw, T., Reidel, Dordrecht.
Press, W. H., Flannery, B. P., Teukolsky, S. A. & Vetterling, W. T., 1986. *Numerical Recipes,* p. 488, Cambridge University Press, Cambridge.
Rose, J. A., 1985. *Astr. J.,* **90,** 1927.
Sarazin, C. L. & O'Connell, R. W., 1983. *Astrophys. J.,* **268,** 552.
Sargent, W. L. W., Schechter, P. L., Boksenberg, A. & Shortridge, K., 1977. *Astrophys. J.,* **212,** 326.
Schombert, J. M., 1987. *Astrophys. J. Suppl.,* **64,** 643.
Schweizer, F., 1980. *Astrophys. J.,* **237,** 303.
Schweizer, F., 1981. *Astrophys. J.,* **246,** 722.
Silk, J., 1976. *Astrophys. J.,* **208,** 646.
Spinrad, H., Smith, H. E. & Taylor, D. J., 1972. *Astrophys. J.,* **175,** 649.
Stone, R. P. S. & Baldwin, J. A., 1983. *Mon. Not. R. astr. Soc.,* **204,** 347.
Strom, K. M. & Strom, S. E., 1978. *Astr. J.,* **83,** 73.
Struble, M. F. & Rood, H. J., 1987. *Astrophys. J. Suppl.,* **63,** 555.
Terlevich, R. J., Davies, R. L., Faber, S. M. & Burstein, D., 1981. *Mon. Not. R. astr. Soc.,* **196,** 381.
Thomsen, B. & Baum, W. A., 1987. *Astrophys. J.,* **315,** 460.
Tifft, W. A., 1969. *Astr. J.,* **74,** 354.
Tinsley, B. M. & Gunn, J. E., 1976. *Astrophys. J.,* **203,** 52.
Tonry, J. L., 1985. *Astr. J.,* **90,** 2431.
Tonry, J. L. & Davis, M., 1979. *Astr. J.,* **84,** 1511.
Toomre, A., 1977. In: *The Evolution of Galaxies and Stellar Populations,* p. 401, eds Tinsley, B. M. & Larson, R. B., Yale University Observatory, New Haven.
VandernBerg, D. A., 1985. *Astrophys. J. Suppl.,* **58,** 711.
White, S. D. M., 1983. *Astrophys. J.,* **274,** 53.
Wirth, A. & Shaw, R., 1983. *Astr. J.,* **88,** 171.
Zinn, R. & West, M. J., 1984. *Astrophys. J. Suppl.,* **55,** 45.

APPENDIX A: ERRORS IN THE LINE-STRENGTH INDICES

Table A1 lists the rms errors derived for our line-strength measurements. For each run the first row gives the errors of the innermost measurements and the second row gives the errors for the outer parts ($r \sim r_e$). The row denoted by the run number 3* gives the errors for the short-exposure galaxies of Run 3. These total errors have been computed by summing three terms in quadrature

$$\sigma^2 = \sigma_{PN}^2 + \sigma_{SK}^2 + \sigma_{SD}^2,$$

where σ_{PN}, σ_{SK} and σ_{SD} are the rms errors from photon noise, sky subtraction and S-distortion, respectively. σ_{PN} has been derived from the mean number of counts in each spectrum as explained in Section 2.2(i); σ_{SK} was set to zero for the inner points and to the values given in Section 2.2(iii) for the outermost points. The comparison of the line-strength indices measured on each side of each galaxy provides a check of our corrections for S-distortion. The mean excess error over σ_{PN} from comparing symmetric points on either side of the nuclei was attributed to residual S-distortion errors (σ_{SD}). In the case of Run 1 we have also included the uncertainties from the Mg_2–Mg_3 calibration.

The errors in the molecular line-strength indices (Mg_1, Mg_2) are dominated by S-distortion in the inner points and to errors in sky subtraction and S-distortion in the outer parts. In the case of atomic indices (Hβ, Fe52, Fe53, Mgb) poor photon statistics are, in most cases, the main contributor to the errors.

Table A1. Observational errors in the line-strength indices.

Run	ΔMg_2	$\Delta H\beta$	$\Delta Fe52$	$\Delta Fe53$	Mgb	ΔMg_1
1	0.017	–	0.19	0.19	0.22	–
	0.031	–	0.45	0.42	0.68	–
2	0.016	0.16	0.11	0.18	0.20	0.053
	0.017	0.60	0.91	1.09	0.29	0.011
3	0.011	0.25	0.37	0.51	0.45	0.043
	0.019	0.42	0.51	0.52	0.64	0.018
3*	0.017	0.37	0.39	0.63	0.30	0.008
4	0.017	-	0.16	0.33	0.28	0.010
	0.027	-	0.31	0.72	0.65	0.045
5	0.009	0.24	0.25	0.24	0.44	0.005
	0.026	0.53	1.00	0.23	0.61	0.006

APPENDIX B: TABLE OF LINE-STRENGTH INDICES

r(″)	Nc	Mg_2	Hβ	Fe52	Fe53	Mgb	Mg_1
NGC 4472 (Major axis) (Run 1)							
0.6	2.18	0.360		2.68 (0.55)	2.57 (0.93)	4.41 (1.11)	
+2.4	1.89	0.341		2.96 (0.60)	2.17 (0.77)	4.30 (1.06)	
−2.4	1.92	0.344		2.96 (0.60)	2.23 (0.79)	4.73 (1.16)	
+4.9	1.40	0.356		2.98 (0.56)	1.86 (0.61)	5.01 (1.15)	
−4.9	1.42	0.376		2.51 (0.47)	1.94 (0.63)	4.70 (1.08)	
+7.4	0.99	0.354		2.85 (0.54)	1.63 (0.53)	5.06 (1.16)	
−7.4	0.99	0.347		3.00 (0.57)	1.82 (0.60)	5.01 (1.15)	
+9.9	0.72	0.318		3.03 (0.57)	2.64 (0.86)	4.42 (1.02)	
−9.9	0.72	0.345		3.28 (0.62)	2.39 (0.78)	4.34 (1.00)	
+12.4	0.56	0.309		2.67 (0.49)	1.82 (0.58)	4.85 (1.09)	
−12.4	0.53	0.364		3.15 (0.58)	2.66 (0.85)	4.42 (0.99)	
+16.1	0.86	0.293		2.75 (0.50)	2.50 (0.77)	4.63 (1.01)	
−16.1	0.84	0.305		2.21 (0.40)	2.05 (0.64)	4.54 (0.99)	
+21.1	0.60	0.289		3.19 (0.51)	2.79 (0.75)	4.94 (0.95)	
−21.1	0.54	0.331		2.29 (0.37)	1.89 (0.51)	4.46 (0.86)	
NGC 4472 (Minor axis) (Run 1)							
0.6	2.46	0.352		2.99 (0.62)	2.67 (0.97)	4.68 (1.18)	
+2.4	2.05	0.345		3.02 (0.57)	2.80 (0.92)	4.73 (1.09)	
−2.4	2.07	0.345		3.11 (0.59)	2.59 (0.85)	4.89 (1.12)	
+4.9	1.42	0.345		2.68 (0.51)	2.15 (0.70)	4.70 (1.08)	
−4.9	1.44	0.360		2.79 (0.53)	2.17 (0.71)	5.00 (1.15)	
+7.4	0.94	0.368		2.90 (0.55)	2.10 (0.69)	4.74 (1.09)	
−7.4	0.95	0.349		2.74 (0.52)	2.33 (0.76)	4.89 (1.12)	
+9.9	0.65	0.348		3.45 (0.65)	2.52 (0.82)	4.82 (1.11)	
−9.9	0.65	0.350		4.21 (0.80)	2.40 (0.79)	4.94 (1.13)	
+13.6	0.89	0.313		3.55 (0.67)	2.11 (0.69)	4.18 (0.96)	
−13.6	0.86	0.353		2.79 (0.53)	2.94 (0.96)	4.81 (1.10)	
+19.7	0.82	0.303		3.01 (0.54)	2.47 (0.77)	4.09 (0.90)	
−19.7	0.78	0.327		2.96 (0.53)	2.22 (0.69)	4.52 (0.99)	
NGC 5813 (Major axis) (Run 1)							
0.6	1.33	0.309		2.94 (0.39)	2.57 (0.55)	5.00 (0.79)	
+2.4	1.00	0.315		2.90 (0.32)	2.88 (0.50)	4.89 (0.64)	
−2.4	1.02	0.318		2.61 (0.29)	3.00 (0.52)	4.68 (0.62)	
+4.9	0.56	0.269		2.82 (0.31)	2.49 (0.43)	4.44 (0.58)	
−4.9	0.56	0.335		3.10 (0.34)	2.59 (0.45)	4.83 (0.64)	
+8.4	0.53	0.231		2.63 (0.31)	2.22 (0.42)	4.31 (0.61)	
−8.4	0.52	0.237		3.19 (0.37)	2.21 (0.41)	3.41 (0.48)	
+16.5	0.55	0.235		2.17 (0.27)	1.79 (0.36)	4.15 (0.62)	
−16.5	0.52	0.230		2.34 (0.29)	1.97 (0.40)	4.25 (0.64)	
NGC 5813 (Minor axis) (Run 1)							
0.6	1.31	0.335		3.03 (0.40)	2.45 (0.53)	4.93 (0.78)	
+2.4	0.97	0.326		3.06 (0.34)	2.77 (0.48)	4.82 (0.63)	
−2.4	0.99	0.337		2.56 (0.28)	2.49 (0.43)	5.05 (0.66)	
+4.9	0.53	0.258		2.08 (0.23)	2.13 (0.37)	4.34 (0.57)	
−4.9	0.54	0.370		3.08 (0.34)	2.65 (0.46)	4.67 (0.61)	
+9.3	0.61	0.236		1.89 (0.24)	2.19 (0.44)	4.60 (0.69)	
−9.3	0.61	0.273		3.30 (0.41)	2.73 (0.55)	4.01 (0.60)	
IC 4296 (Major axis) (Run 1)							
0.6	1.76	0.356		2.89 (0.55)	2.10 (0.69)	4.69 (1.08)	
+2.4	1.37	0.360		2.80 (0.51)	2.16 (0.67)	4.63 (1.01)	
−2.4	1.38	0.356		2.94 (0.53)	2.00 (0.62)	4.67 (1.02)	
+4.9	0.75	0.340		2.67 (0.48)	2.27 (0.70)	4.57 (1.00)	
−4.9	0.77	0.329		2.84 (0.51)	1.80 (0.56)	4.84 (1.06)	
+8.4	0.71	0.265		2.96 (0.53)	2.44 (0.76)	3.85 (0.84)	
−8.4	0.69	0.256		2.93 (0.53)	1.10 (0.34)	3.89 (0.85)	
+15.5	0.59	0.246		2.59 (0.45)	1.96 (0.57)	3.99 (0.83)	
−15.5	0.56	0.239		3.21 (0.55)	2.05 (0.60)	3.73 (0.78)	
IC 4296 (Minor axis) (Run 1)							
0.6	1.70	0.362		3.42 (0.65)	2.37 (0.78)	4.86 (1.12)	
+2.4	1.26	0.330		3.03 (0.55)	2.07 (0.64)	4.78 (1.05)	
−2.4	1.28	0.353		3.24 (0.58)	2.17 (0.67)	4.87 (1.07)	
+4.9	0.69	0.310		2.67 (0.48)	2.55 (0.79)	4.51 (0.99)	
−4.9	0.69	0.335		2.28 (0.41)	1.78 (0.55)	4.63 (1.01)	
+8.4	0.63	0.274		2.15 (0.39)	2.36 (0.73)	4.21 (0.92)	
−8.4	0.61	0.262		1.88 (0.32)	1.64 (0.48)	4.07 (0.85)	
+15.5	0.50	0.217		1.68 (0.29)	2.07 (0.61)	4.69 (0.98)	
−15.5	0.49	0.263		3.27 (0.56)	1.33 (0.39)	4.57 (0.95)	
NGC 5813 (Run 2)							
0.6	17.60	0.318	0.99 (−0.12)	2.84 (0.38)	2.30 (0.50)	4.61 (0.73)	0.180
+2.3	12.10	0.298	1.11 (−0.11)	2.82 (0.31)	2.56 (0.45)	4.38 (0.58)	0.143
−2.3	12.30	0.321	1.33 (−0.11)	2.66 (0.29)	2.30 (0.40)	4.10 (0.54)	0.218
+4.7	5.84	0.266	1.28 (−0.11)	2.56 (0.28)	2.56 (0.45)	4.02 (0.53)	0.120
−4.7	6.04	0.299	1.43 (−0.11)	2.34 (0.26)	2.37 (0.41)	3.80 (0.50)	0.198
+7.1	3.46	0.246	1.40 (−0.12)	2.22 (0.26)	2.08 (0.39)	3.93 (0.55)	0.111

Table B1 – *continued.*

r(″)	Nc	Mg_2	Hβ	Fe52	Fe53	Mgb	Mg_1
			NGC 5813 (Run 2) Contd.				
−7.1	3.51	0.272	1.54 (−0.12)	2.12 (0.25)	2.05 (0.38)	3.75 (0.53)	0.169
+9.5	2.41	0.239	1.43 (−0.12)	2.23 (0.29)	2.01 (0.43)	3.87 (0.61)	0.111
−9.5	2.38	0.256	1.63 (−0.12)	2.40 (0.32)	2.28 (0.49)	3.55 (0.56)	0.154
+11.9	1.85	0.229	1.34 (−0.12)	2.34 (0.31)	1.81 (0.39)	3.35 (0.53)	0.107
−11.9	1.83	0.247	1.58 (−0.12)	2.38 (0.31)	2.46 (0.53)	3.51 (0.56)	0.128
+14.4	1.49	0.226	1.33 (−0.12)	2.64 (0.35)	1.93 (0.42)	3.47 (0.55)	0.105
−14.4	1.48	0.234	1.75 (−0.12)	2.05 (0.27)	2.02 (0.43)	3.57 (0.57)	0.129
+16.8	1.25	0.217	1.32 (−0.12)	2.37 (0.31)	2.79 (0.60)	3.66 (0.58)	0.107
−16.8	1.24	0.218	1.46 (−0.12)	2.36 (0.31)	1.59 (0.34)	3.32 (0.53)	0.122
+19.2	1.08	0.219	1.62 (−0.12)	2.28 (0.28)	2.81 (0.56)	3.86 (0.58)	0.104
−19.2	1.06	0.211	1.71 (−0.12)	2.46 (0.31)	1.14 (0.23)	3.41 (0.51)	0.125
+21.6	0.95	0.210	1.88 (−0.12)	2.16 (0.25)	2.20 (0.41)	3.22 (0.45)	0.101
−21.6	0.93	0.205	1.43 (−0.12)	2.62 (0.31)	1.44 (0.27)	3.20 (0.45)	0.115
+24.0	0.85	0.202	2.04 (−0.12)	2.24 (0.26)	2.54 (0.48)	2.85 (0.40)	0.110
−24.0	0.82	0.203	1.20 (−0.12)	2.34 (0.27)	1.49 (0.28)	3.09 (0.43)	0.100
+26.4	0.77	0.185	1.54 (−0.11)	1.98 (0.22)	1.69 (0.29)	3.08 (0.41)	0.095
−26.4	0.74	0.202	1.32 (−0.11)	1.76 (0.19)	0.82 (0.14)	3.33 (0.44)	0.107
+28.8	0.71	0.170	1.62 (−0.11)	2.29 (0.25)	1.94 (0.34)	2.76 (0.36)	0.095
−28.8	0.67	0.189	1.67 (−0.11)	1.08 (0.12)	1.09 (0.19)	2.64 (0.35)	0.111
+31.2	0.66	0.181	1.49 (−0.11)	1.93 (0.21)	1.64 (0.29)	2.63 (0.35)	0.103
−31.2	0.61	0.193	1.57 (−0.11)	1.25 (0.14)	1.33 (0.23)	2.22 (0.29)	0.110
+33.6	0.60	0.195	1.77 (−0.11)	1.89 (0.19)	1.88 (0.30)	2.89 (0.36)	0.095
−33.6	0.56	0.197	0.78 (−0.11)	2.25 (0.23)	2.46 (0.40)	2.72 (0.33)	0.102
+36.0	0.56	0.173	1.69 (−0.11)	2.05 (0.21)	2.18 (0.35)	2.43 (0.30)	0.090
−36.0	0.52	0.180	0.90 (−0.11)	1.52 (0.16)	1.47 (0.24)	2.93 (0.36)	0.096
+39.6	0.99	0.176	0.99 (−0.11)	2.91 (0.30)	1.48 (0.24)	2.84 (0.35)	0.090
−39.6	0.93	0.172	1.97 (−0.11)	1.35 (0.14)	2.32 (0.37)	2.98 (0.37)	0.092
+44.4	0.85	0.160	1.98 (−0.11)	2.00 (0.21)	1.08 (0.17)	2.46 (0.30)	0.092
−44.4	0.78	0.158	1.68 (−0.11)	2.32 (0.24)	2.92 (0.47)	2.99 (0.37)	0.077
+49.2	0.75	0.128	1.87 (−0.11)	1.00 (0.10)	0.42 (0.07)	1.84 (0.23)	0.072
−49.2	0.70	0.162	1.59 (−0.11)	2.01 (0.21)	1.63 (0.26)	3.65 (0.45)	0.066
+54.0	0.64	0.151	2.81 (−0.11)	1.90 (0.20)	0.93 (0.15)	1.75 (0.22)	0.077
−54.0	0.61	0.123	1.24 (−0.11)	1.43 (0.15)	2.26 (0.36)	2.74 (0.34)	0.076
+58.8	0.57	0.141	1.04 (−0.11)	2.14 (0.22)	1.13 (0.18)	1.62 (0.20)	0.079
−58.8	0.54	0.116	2.07 (−0.11)	2.50 (0.26)	2.60 (0.42)	2.84 (0.35)	0.069
+64.7	0.74	0.109	1.58 (−0.11)	1.52 (0.15)	2.18 (0.32)	1.20 (0.14)	0.076
−64.7	0.71	0.111	1.58 (−0.11)	2.05 (0.20)	1.93 (0.29)	1.81 (0.21)	0.066
+71.9	0.64	0.083	1.24 (−0.11)	1.08 (0.10)	2.03 (0.30)	1.35 (0.15)	0.053
−71.9	0.60	0.110	1.94 (−0.11)	0.78 (0.08)	2.24 (0.33)	1.74 (0.20)	0.057
+79.1	0.55	0.115	1.26 (−0.10)	3.45 (0.31)	1.59 (0.22)	1.30 (0.14)	0.069
−79.1	0.52	0.077	1.03 (−0.10)	0.99 (0.09)	1.37 (0.19)	1.05 (0.11)	0.081
+88.7	0.79	0.096	2.14 (−0.10)	1.62 (0.15)	3.41 (0.47)	1.31 (0.14)	0.075
−88.7	0.79	0.090	0.79 (−0.10)	1.73 (0.15)	0.57 (0.08)	1.63 (0.17)	0.056
			NGC 3818 (Run 3)				
0.6	7.89	0.364	1.38 (−0.11)	3.33 (0.35)	3.05 (0.51)	4.92 (0.63)	0.203
+2.2	3.88	0.298	1.35 (−0.10)	3.39 (0.30)	2.93 (0.40)	4.80 (0.51)	0.161
−2.2	3.93	0.280	1.47 (−0.10)	2.63 (0.24)	2.95 (0.40)	4.59 (0.49)	0.082
+4.6	1.35	0.262	1.11 (−0.10)	2.60 (0.20)	2.99 (0.34)	4.16 (0.38)	0.151
−4.6	1.35	0.253	1.67 (−0.10)	2.58 (0.20)	2.44 (0.28)	4.50 (0.41)	0.089
+7.1	0.72	0.253	1.28 (−0.08)	2.46 (0.14)	2.31 (0.19)	3.98 (0.27)	0.133
−7.1	0.75	0.263	1.39 (−0.08)	2.91 (0.17)	2.02 (0.17)	4.41 (0.30)	0.113
+10.5	0.78	0.255	1.35 (−0.08)	2.63 (0.15)	2.56 (0.20)	4.53 (0.30)	0.121
−10.5	0.79	0.251	1.79 (−0.08)	3.05 (0.17)	2.46 (0.19)	3.91 (0.26)	0.099
+16.3	0.54	0.254	1.18 (−0.08)	1.40 (0.08)	1.52 (0.12)	3.89 (0.25)	0.113
−16.3	0.54	0.225	1.75 (−0.08)	1.58 (0.09)	0.66 (0.05)	3.18 (0.21)	0.097
			NGC 3904 (Run 3)				
0.6	8.11	0.366	1.53 (−0.11)	3.26 (0.35)	3.03 (0.51)	4.47 (0.57)	0.202
+2.2	4.60	0.275	1.69 (−0.11)	3.05 (0.31)	2.73 (0.44)	4.69 (0.58)	0.076
−2.2	4.53	0.275	1.56 (−0.11)	2.90 (0.30)	2.48 (0.40)	4.76 (0.59)	0.141
+4.7	1.68	0.238	0.91 (−0.11)	2.82 (0.28)	1.88 (0.29)	4.00 (0.48)	0.086
−4.7	1.83	0.253	1.84 (−0.11)	2.61 (0.26)	1.95 (0.30)	4.15 (0.49)	0.126
+7.1	0.97	0.233	1.95 (−0.11)	3.30 (0.35)	2.20 (0.37)	3.51 (0.45)	0.090
−7.1	1.04	0.239	2.21 (−0.11)	2.55 (0.27)	1.90 (0.32)	4.04 (0.51)	0.112
+9.5	0.65	0.243	1.35 (−0.11)	3.24 (0.35)	2.47 (0.41)	3.68 (0.47)	0.086
−9.5	0.67	0.242	2.09 (−0.11)	2.49 (0.27)	2.50 (0.42)	3.81 (0.49)	0.115
+12.9	0.78	0.245	1.84 (−0.11)	3.73 (0.36)	1.87 (0.28)	3.87 (0.44)	0.080
−12.9	0.79	0.251	1.73 (−0.11)	2.74 (0.26)	2.31 (0.34)	3.90 (0.45)	0.110
+18.8	0.58	0.230	1.12 (−0.11)	3.13 (0.30)	2.31 (0.34)	3.24 (0.37)	0.070
−18.8	0.60	0.231	0.83 (−0.11)	2.32 (0.22)	1.28 (0.19)	3.87 (0.44)	0.104
+29.4	0.51	0.235	1.79 (−0.10)	3.27 (0.28)	2.77 (0.36)	3.94 (0.40)	0.086
−29.4	0.58	0.251	1.35 (−0.10)	2.15 (0.19)	1.59 (0.21)	3.23 (0.33)	0.075
			NGC 4478 (Run 3)				
0.6	5.33	0.254	1.80 (−0.09)	3.56 (0.26)	3.41 (0.37)	4.31 (0.37)	0.101
+2.3	3.78	0.239	1.58 (−0.09)	3.03 (0.22)	2.77 (0.30)	4.29 (0.37)	0.078
−2.3	3.72	0.265	1.77 (−0.09)	3.45 (0.25)	2.82 (0.31)	4.56 (0.40)	0.133
+4.7	1.98	0.244	1.45 (−0.09)	2.56 (0.18)	2.56 (0.26)	4.59 (0.38)	0.081

Table B1 – *continued.*

r(″)	Nc	Mg_2	Hβ	Fe52	Fe53	Mgb	Mg_1
			NGC 4478 (Run 3) Contd.				
−4.7	2.09	0.238	1.83 (−0.09)	3.09 (0.22)	2.83 (0.29)	4.19 (0.35)	0.119
+7.1	1.21	0.228	1.59 (−0.09)	3.05 (0.21)	1.90 (0.19)	4.19 (0.33)	0.079
−7.1	1.30	0.239	1.56 (−0.09)	3.19 (0.21)	2.80 (0.27)	3.68 (0.29)	0.114
+9.5	0.82	0.230	2.07 (−0.09)	3.01 (0.19)	2.41 (0.22)	4.05 (0.31)	0.089
−9.5	0.87	0.243	1.69 (−0.09)	3.31 (0.21)	2.88 (0.27)	4.03 (0.31)	0.114
+11.9	0.57	0.235	1.42 (−0.08)	2.74 (0.16)	2.59 (0.22)	4.33 (0.30)	0.079
−11.9	0.59	0.251	1.76 (−0.08)	3.36 (0.20)	2.26 (0.19)	3.69 (0.25)	0.125
+15.3	0.69	0.219	1.31 (−0.08)	2.73 (0.14)	2.23 (0.16)	3.45 (0.21)	0.089
−15.3	0.72	0.244	2.23 (−0.08)	3.38 (0.18)	1.84 (0.14)	3.90 (0.24)	0.135
+21.9	0.56	0.213	1.47 (−0.07)	2.21 (0.09)	2.72 (0.15)	3.22 (0.16)	0.075
−21.9	0.60	0.245	1.89 (−0.07)	3.79 (0.16)	2.87 (0.16)	3.64 (0.18)	0.122
			NGC 4742 (Run 3)				
0.6	0.75	0.231	3.82 (−0.08)	2.85 (0.15)	2.37 (0.17)	3.33 (0.21)	0.114
+2.1	0.41	0.149	3.72 (−0.06)	3.33 (0.12)	3.82 (0.18)	4.39 (0.19)	0.025
−2.1	0.39	0.158	3.80 (−0.06)	1.43 (0.05)	0.13 (0.01)	0.94 (0.04)	0.073
+4.5	1.88	0.183	1.81 (−0.05)	2.98 (0.09)	3.98 (0.15)	3.35 (0.11)	0.082
−4.5	2.33	0.159	2.74 (−0.05)	2.56 (0.07)	1.05 (0.04)	1.93 (0.06)	0.078
+7.1	0.78	0.168	1.66 (−0.05)	2.85 (0.08)	2.02 (0.07)	3.07 (0.09)	0.069
−7.1	0.96	0.173	2.43 (−0.05)	2.64 (0.07)	1.69 (0.06)	2.56 (0.08)	0.071
+9.5	0.48	0.165	2.17 (−0.05)	2.51 (0.07)	2.01 (0.07)	3.09 (0.09)	0.063
−9.5	0.55	0.183	2.13 (−0.05)	1.95 (0.05)	1.21 (0.04)	2.91 (0.09)	0.079
+12.9	0.59	0.165	2.31 (−0.04)	1.93 (0.04)	2.70 (0.07)	3.11 (0.08)	0.061
−12.9	0.65	0.166	1.84 (−0.04)	2.64 (0.06)	1.03 (0.03)	2.69 (0.07)	0.068
+19.7	0.53	0.172	2.30 (−0.03)	2.24 (0.04)	2.55 (0.05)	3.29 (0.06)	0.054
−19.7	0.61	0.176	1.32 (−0.03)	2.44 (0.04)	0.35 (0.01)	2.84 (0.06)	0.078
			NGC 5638 (Run 3)				
0.6	2.01	0.319	1.41 (−0.10)	3.52 (0.28)	2.72 (0.32)	4.96 (0.47)	0.161
+2.3	1.43	0.299	1.94 (−0.10)	3.23 (0.27)	3.01 (0.38)	4.98 (0.49)	0.141
−2.3	1.43	0.306	1.60 (−0.10)	3.31 (0.27)	2.50 (0.31)	4.75 (0.47)	0.163
+4.7	0.70	0.279	2.26 (−0.10)	3.42 (0.26)	2.45 (0.28)	4.54 (0.41)	0.143
−4.7	0.70	0.291	1.82 (−0.10)	2.72 (0.21)	2.61 (0.30)	4.30 (0.39)	0.153
+8.0	0.66	0.256	1.75 (−0.09)	3.55 (0.25)	3.05 (0.31)	3.65 (0.30)	0.127
−8.0	0.63	0.312	1.02 (−0.09)	2.65 (0.19)	1.68 (0.17)	5.05 (0.42)	0.144
+15.5	0.58	0.254	1.63 (−0.08)	2.78 (0.16)	2.04 (0.17)	3.84 (0.26)	0.128
−15.5	0.52	0.265	1.94 (−0.08)	3.73 (0.22)	2.67 (0.22)	3.67 (0.25)	0.138
			NGC 5831 (Run 3)				
0.6	4.14	0.301	1.50 (−0.10)	3.73 (0.29)	3.35 (0.38)	4.22 (0.38)	0.133
+2.2	2.35	0.261	1.71 (−0.10)	3.36 (0.27)	3.05 (0.36)	4.79 (0.45)	0.078
−2.2	2.34	0.291	2.01 (−0.10)	3.54 (0.28)	2.94 (0.35)	4.84 (0.46)	0.160
+4.6	0.90	0.271	1.68 (−0.10)	2.99 (0.23)	2.58 (0.29)	4.25 (0.39)	0.093
−4.6	0.93	0.237	1.85 (−0.10)	3.01 (0.23)	2.49 (0.28)	4.36 (0.40)	0.106
+7.1	0.49	0.252	1.28 (−0.09)	3.25 (0.23)	2.14 (0.22)	4.01 (0.33)	0.076
−7.1	0.50	0.255	1.92 (−0.09)	3.50 (0.25)	1.83 (0.19)	4.12 (0.34)	0.118
+10.5	0.56	0.226	1.12 (−0.09)	2.71 (0.17)	2.02 (0.19)	4.14 (0.31)	0.078
−10.5	0.56	0.222	1.12 (−0.09)	3.36 (0.22)	1.94 (0.18)	3.42 (0.26)	0.102
+17.9	0.52	0.206	1.71 (−0.08)	2.92 (0.15)	1.23 (0.09)	2.68 (0.17)	0.059
−17.9	0.54	0.214	1.48 (−0.08)	1.77 (0.09)	1.73 (0.13)	2.99 (0.18)	0.101
			NGC 5845 (Run 3)				
0.6	8.57	0.325	1.65 (−0.12)	3.22 (0.51)	2.57 (0.69)	4.65 (0.90)	0.165
+2.2	4.92	0.301	1.46 (−0.11)	3.07 (0.34)	2.94 (0.51)	4.68 (0.62)	0.167
−2.2	4.89	0.281	1.60 (−0.11)	2.72 (0.30)	2.39 (0.42)	4.26 (0.56)	0.093
+4.6	1.58	0.290	1.51 (−0.10)	3.06 (0.27)	2.87 (0.39)	4.44 (0.47)	0.182
−4.6	1.50	0.264	1.42 (−0.10)	2.75 (0.25)	2.31 (0.32)	4.20 (0.45)	0.087
+7.0	0.60	0.275	1.34 (−0.09)	2.82 (0.17)	2.69 (0.24)	4.57 (0.33)	0.152
−7.0	0.59	0.270	1.06 (−0.09)	3.19 (0.20)	3.02 (0.27)	3.70 (0.27)	0.104
+11.0	0.55	0.252	1.27 (−0.07)	2.48 (0.12)	2.34 (0.15)	4.48 (0.25)	0.140
−11.0	0.54	0.269	1.43 (−0.07)	2.04 (0.10)	2.80 (0.18)	4.00 (0.22)	0.129
			NGC 3136 (Run 3)				
0.6	0.71	0.302	1.95 (−0.12)	3.10 (0.46)	2.33 (0.57)	4.42 (0.79)	0.152
+3.1	0.56	0.259	1.77 (−0.12)	3.24 (0.42)	3.23 (0.67)	4.06 (0.63)	0.120
−3.1	0.55	0.293	1.99 (−0.12)	2.39 (0.31)	2.12 (0.44)	4.15 (0.64)	0.158
			NGC 3605 (Run 3)				
1.5	0.78	0.237	2.24 (−0.07)	3.46 (0.14)	2.51 (0.14)	4.27 (0.21)	0.104
			NGC 3608 (Run 3)				
0.6	0.87	0.352	1.65 (−0.11)	3.18 (0.35)	3.19 (0.55)	5.66 (0.75)	0.176
+3.1	0.52	0.321	1.22 (−0.10)	3.52 (0.30)	4.31 (0.56)	4.17 (0.43)	0.156
−3.1	0.54	0.293	1.92 (−0.10)	2.86 (0.25)	1.68 (0.22)	4.64 (0.48)	0.151
			NGC 3923 (Run 3)				
0.6	0.75	0.334	2.59 (−0.12)	3.54 (0.55)	2.58 (0.67)	5.12 (0.96)	0.144
+2.3	0.51	0.314	1.05 (−0.12)	3.42 (0.52)	2.32 (0.59)	3.94 (0.72)	0.177
−2.3	0.50	0.339	1.72 (−0.12)	3.88 (0.59)	2.66 (0.67)	4.62 (0.85)	0.190
+6.6	0.59	0.318	1.52 (−0.12)	3.44 (0.45)	2.05 (0.44)	4.30 (0.68)	0.156
−6.6	0.60	0.315	1.34 (−0.12)	3.72 (0.49)	3.05 (0.66)	4.07 (0.65)	0.162
			NGC 3962 (Run 3)				
0.6	0.73	0.302	1.49 (−0.12)	2.82 (0.35)	2.18 (0.44)	5.40 (0.81)	0.125
+3.1	0.51	0.326	1.30 (−0.12)	3.48 (0.45)	2.70 (0.56)	4.66 (0.72)	0.178

Table B1 – *continued.*

r(″)	Nc	Mg_2	Hβ	Fe52	Fe53	Mgb	Mg_1
			NGC 3962 (Run 3) Contd.				
−3.1	0.51	0.323	1.15 (−0.12)	2.73 (0.35)	2.26 (0.47)	4.82 (0.74)	0.184
			NGC 4458 (Run 3)				
0.6	0.54	0.277	1.59 (−0.07)	3.00 (0.14)	3.03 (0.20)	4.13 (0.23)	0.132
+4.8	0.49	0.225	1.57 (−0.07)	2.42 (0.11)	2.69 (0.17)	4.21 (0.23)	0.081
−4.8	0.49	0.191	1.38 (−0.07)	2.66 (0.13)	2.14 (0.14)	4.03 (0.22)	0.078
			NGC 4476 (Run 3)				
1.6	0.70	0.155	2.31 (−0.06)	2.84 (0.10)	2.06 (0.09)	3.49 (0.14)	0.045
			NGC 4489 (Run 3)				
1.5	0.79	0.213	2.50 (−0.04)	3.43 (0.07)	2.32 (0.06)	3.88 (0.10)	0.088
			IC 4329 (Run 4)				
0.6	1.66	0.420		4.33 (0.86)	3.81 (1.31)	4.57 (1.10)	0.250
+2.4	1.08	0.355		3.73 (0.64)	1.70 (0.50)	4.47 (0.93)	0.178
−2.4	1.22	0.320		3.44 (0.59)	2.49 (0.73)	3.86 (0.80)	0.158
+4.9	0.51	0.279		3.51 (0.73)	2.38 (0.86)	4.02 (1.01)	0.123
−4.9	0.61	0.361		3.61 (0.75)	3.24 (1.18)	3.88 (0.98)	0.183
+8.4	0.51	0.308		2.29 (0.47)	1.53 (0.56)	4.35 (1.10)	0.107
−8.4	0.59	0.330		4.42 (0.91)	1.92 (0.70)	4.19 (1.06)	0.183
+15.7	0.57	0.288		2.34 (0.42)	1.61 (0.50)	4.19 (0.92)	0.126
−15.7	0.59	0.297		3.61 (0.65)	2.06 (0.64)	4.20 (0.92)	0.138
+29.0	0.56	0.317		2.80 (0.51)	1.63 (0.50)	6.03 (1.32)	0.125
−29.0	0.60	0.331		2.77 (0.50)	2.05 (0.64)	4.94 (1.08)	0.185
			NGC 4382 (Run 4)				
+2.4	10.60	0.248		3.80 (0.37)	3.56 (0.53)	4.52 (0.52)	0.081
−2.4	12.40	0.260		3.93 (0.38)	3.40 (0.51)	4.34 (0.50)	0.073
+4.9	4.44	0.245		2.32 (0.24)	2.66 (0.43)	3.62 (0.45)	0.114
−4.9	5.99	0.242		2.68 (0.28)	2.51 (0.40)	3.73 (0.46)	0.089
+7.4	2.68	0.221		2.74 (0.28)	2.34 (0.38)	3.71 (0.46)	0.086
−7.4	3.42	0.234		2.69 (0.28)	1.40 (0.23)	3.95 (0.49)	0.088
+9.9	1.98	0.233		2.40 (0.25)	1.59 (0.26)	3.68 (0.45)	0.085
−9.9	2.28	0.263		2.76 (0.28)	2.89 (0.47)	3.62 (0.45)	0.096
+12.4	1.49	0.222		2.61 (0.27)	1.36 (0.22)	2.96 (0.36)	0.081
−12.4	1.64	0.254		2.53 (0.26)	3.38 (0.54)	3.01 (0.37)	0.078
+15.0	1.17	0.238		2.78 (0.29)	1.59 (0.26)	3.61 (0.44)	0.095
−15.0	1.26	0.237		2.14 (0.22)	2.33 (0.38)	3.23 (0.40)	0.096
+17.5	0.96	0.250		2.22 (0.23)	1.92 (0.31)	3.77 (0.46)	0.092
−17.5	1.02	0.226		2.09 (0.22)	2.40 (0.39)	3.82 (0.47)	0.102
+20.0	0.82	0.236		2.75 (0.28)	2.15 (0.35)	3.66 (0.45)	0.084
−20.0	0.85	0.219		2.14 (0.22)	2.81 (0.45)	3.82 (0.47)	0.086
+22.4	0.72	0.246		3.31 (0.34)	1.64 (0.26)	3.78 (0.47)	0.071
−22.4	0.73	0.230		2.97 (0.31)	1.91 (0.31)	3.17 (0.39)	0.095
+25.0	0.64	0.235		2.75 (0.28)	1.62 (0.26)	3.47 (0.43)	0.078
−25.0	0.64	0.235		2.69 (0.28)	1.98 (0.32)	2.95 (0.36)	0.105
+27.5	0.57	0.227		3.10 (0.32)	3.35 (0.54)	2.82 (0.35)	0.087
−27.5	0.59	0.233		2.48 (0.26)	2.62 (0.42)	3.50 (0.43)	0.093
+30.0	0.52	0.214		2.52 (0.26)	3.15 (0.51)	2.89 (0.36)	0.076
−30.0	0.53	0.230		3.48 (0.36)	1.44 (0.23)	3.52 (0.43)	0.088
+33.7	0.93	0.219		2.21 (0.23)	2.38 (0.38)	2.58 (0.32)	0.055
−33.7	0.93	0.207		2.13 (0.22)	2.12 (0.34)	2.66 (0.33)	0.102
+38.7	0.85	0.225		2.11 (0.22)	2.04 (0.33)	3.18 (0.39)	0.050
−38.7	0.81	0.223		2.30 (0.24)	2.03 (0.33)	2.71 (0.33)	0.120
+43.7	0.70	0.203		2.44 (0.25)	0.82 (0.13)	3.88 (0.48)	0.054
−43.7	0.72	0.240		2.02 (0.21)	3.42 (0.55)	3.53 (0.43)	0.141
+48.7	0.61	0.184		1.93 (0.20)	2.56 (0.41)	3.04 (0.37)	0.055
−48.7	0.71	0.252		1.95 (0.20)	1.89 (0.30)	3.10 (0.38)	0.149
			0559−40 (Run 5)				
1.1	2.46	0.316	1.68 (−0.12)	2.39 (0.41)		4.64 (0.97)	0.153
+4.4	1.34	0.299	1.72 (−0.12)	2.38 (0.43)		4.17 (0.91)	0.154
−4.4	1.27	0.302	2.12 (−0.12)	2.02 (0.36)		5.09 (1.11)	0.157
+10.8	0.70	0.245	2.39 (−0.12)	1.74 (0.30)		2.61 (0.54)	0.131
−10.8	0.72	0.281	2.87 (−0.12)	0.33 (0.06)		3.81 (0.79)	0.118
			PKS 2354−35 (Run 5)				
1.1	2.07	0.285	−0.07 (−0.12)			4.73 (1.09)	0.142
+4.4	1.28	0.275	0.83 (−0.12)			4.30 (0.99)	0.132
−4.4	1.36	0.287	0.97 (−0.12)			5.08 (1.17)	0.132
+9.2	0.62	0.256	1.53 (−0.12)			3.94 (0.90)	0.112
−9.2	0.63	0.277	0.84 (−0.12)			4.37 (1.00)	0.102
+15.8	0.64	0.250	1.54 (−0.12)			4.04 (1.02)	0.104
−15.8	0.65	0.273	0.42 (−0.12)			3.69 (0.93)	0.106
			Sersic 40/6 (Run 5)				
1.1	3.25	0.287	1.30 (−0.12)		2.01 (0.77)	4.15 (1.09)	0.136
+4.7	1.93	0.263	1.67 (−0.10)		1.74 (0.91)	3.76 (1.31)	0.119
−4.3	1.35	0.283	1.37 (−0.11)		1.40 (0.62)	3.96 (1.18)	0.124
+9.2	2.67	0.278	1.97 (−0.12)		1.68 (0.39)	4.02 (0.68)	0.127
−10.9	0.72	0.246	1.36 (0.00)		0.47 (0.42)	3.40 (1.93)	0.109
+13.6	0.60	0.227	1.98 (−0.12)		0.94 (0.28)	2.80 (0.58)	0.096
−22.9	0.61	0.247	1.60 (0.03)		1.12 (1.11)	2.66 (1.64)	0.088